Journal of Materials Science & Technology 142 (2023) 60–75

Contents lists available at ScienceDirect

Journal of Materials Science & Technology

journal homepage: www.elsevier.com/locate/jmst

Research Article

Unconventional dislocation starvation behavior of medium-entropy alloy single crystal pillars containing pre-existing dislocations

Luling Wang[a,b], Bin Liu[a], Jianqiu Zhou[a,*], Yang Cao[b,*], Feng Zhang[a,c], Yonghao Zhao[b,*]

[a] Department of Mechanical and Power Engineering, Nanjing Tech University, Nanjing 210009, China
[b] Nano and Heterogeneous Materials Center, School of Materials Science and Engineering, Nanjing University of Science and Technology, Nanjing 210094, China
[c] School of Mechanical Engineering, Nanjing Institute of Technology, Nanjing 211167, China

ARTICLE INFO

Article history:
Received 23 June 2022
Revised 22 July 2022
Accepted 23 July 2022
Available online 6 November 2022

Keywords:
Molecular dynamics
Medium entropy alloy
Single crystal pillar
Dislocation starvation
Chemical short-range order
Size effect

ABSTRACT

The excellent dislocation storage ability of bulk multi-principal element alloys (MPEAs) has been widely reported. To date, however, the underlying mechanisms of dislocation escape behavior in small-size face-centered cubic (FCC) MPEAs have rarely been studied. Here, we quantitatively control the initial dislocation densities ($\sim10^{15}$ m^{-2} and $\sim10^{16}$ m^{-2}) by large-scale molecular dynamics (MD) simulations and perform uniaxial compression simulations to compare the dislocation starvation behavior of CrCoNi with pure Cu single crystal pillars (SCPs). The analysis reveals that the CrCoNi SCPs with low initial dislocation density ($\sim10^{15}$ m^{-2}) can continuously accommodate mobile dislocations, and the critical dimension for dislocation starvation is about 30 nm. In particular, the CrCoNi SCPs with chemical short-range ordering (SRO) exhibit better dislocation storage and multiplication abilities than the random solid solution (RSS) samples even when the initial dislocation density is low. However, the presence of a large number of pre-existing dislocation locks governs the strong dislocation multiplication ability of the small-size RSS CrCoNi SCPs, in obvious contrast to the deformation of all pure Cu SCPs which is completely dominated by intermittent mobile dislocation starvation. Most importantly, we reveal the fundamental physics for the good dislocation storage of CrCoNi SCPs at small sizes from the perspective of chemical heterogeneity. The new phenomena reported in this work provide a unique atomic-scale perspective for understanding the microscopic physical origin of the mechanical behavior of MPEAs and the discovery of extremely slow dislocation escape behavior in small-scaled pillars, providing a reliable basis for the development of the dislocation starvation model.

1. Introduction

"Smaller is stronger" is prominent in micron and submicron single crystals [1,2]. The strength of some nanowires can even approach the theoretical value [3–6]. Dating back to the early 21st century, the size effect was revealed by performing uniaxial compression tests on micropillars with diameters in micrometers and sub-micrometers [7]. Unlike the bulk materials, the compressive stress–strain curves for the single crystal micropillars were not continuous, but with pronounced intermittency [8–10]. Greer and co-workers [11] proposed a dislocation starvation model to explain the discontinuous plastic behavior of submicron-sized single crystal pillars (SCPs). This model suggests that dislocations escape from the free surface easily when the sample size is small enough. Correspondingly, the dislocation multiplication rate is lower than the annihilation rate, resulting in decreased dislocation density and even dislocation starvation. The intermittent plastic deformation can only be driven by repeated surface dislocation nucleation. The dislocation starvation model has been justified by in-suit compression experiments [12,13]. The classical dislocation starvation model has been demonstrated in pure metals and conventional alloys with dilute elemental concentrations [14,15], but has not been well studied in multi-principal element alloys (MPEAs).

In the early years, researchers focused on high-entropy alloys (HEAs) with five or more principal elements [16,17] for their outstanding thermal stability [18], strength, hardness [19,20], fatigue properties, wear resistance [21,22], etc. Later, Gludovatz et al. [23] successfully prepared the CrCoNi medium-entropy alloy (MEA), which also had excellent mechanical properties. Researchers have attributed the excellent mechanical properties of

* Corresponding authors.
E-mail addresses: zhouj@njtech.edu.cn (J. Zhou), y.cao@njust.edu.cn (Y. Cao), yhzhao@njust.edu.cn (Y. Zhao).

https://doi.org/10.1016/j.jmst.2022.07.065
1005-0302/

HEAs and MEAs to their unique dislocation activities [24–26]. Yang et al. [27] found that dislocations move on an average speed of $\sim 10^{-8}$ m s^{-1} (significantly slower than that in pure FCC metals) while performing the shear stress of ~200 MPa, in $Al_{0.1}CoCrFeNi$ HEA nanopillars. In addition, they also found that dislocations tend to accumulate inside the HEA SCPs [27] rather than quickly escaping from the surface [8]. Giwa et al. [28] observed that dislocation densities in the deformed HEAs submicron pillars were significantly higher than in pure metals. However, accurate capture of the dislocation activities by *in-situ* TEM and SEM is difficult due to the intrinsic instrumental noise in the detection equipment [29], especially at high strain rates. Besides, it is also difficult to accurately measure the dislocation density in the area damaged by the focused ion beam (FIB) [1]. Thus, detailed insight into the physical origin of the deformation behavior for the MPEA SCPs is still in demand.

Chemical short-range order (SRO) is considered an important factor that causes the unique dislocation behavior of MPEAs [30,31]. Our previous work shows that local chemical order plays a crucial role in preventing dislocation glide and increasing dislocation storage in $Ni_2Co_1Fe_1V_{0.5}Mo_{0.2}$ MEA. However, direct visualization of SRO is still a conundrum, which requires advanced compositional characterization techniques, such as high-angle annular dark-field (HAADF) imaging [32,33] and three-dimensional atom probe tomography (3D-APT) [34].

As an alternative approach, molecular dynamics (MD) simulation provides good insight into the relationship between chemical SRO and mechanical behaviors of alloys [35–37]. Besides, the proper MD simulations can provide unique insights for *in-situ* observation [38–40]. So far, many atomic simulations devoted to plastic behaviors of the single crystal samples free of pre-existing dislocations, resulting in an apparent deviation from the actual experimental results. For example, extremely high stress close to theoretical strength [41] and intermittent strain bursts significantly below the initial yield stress [42, 43] have been revealed by atomic simulations. Jennings et al. [44] argued that pre-existing defect is an indispensable factor for realistic SCPs to reflect the size effects.

In this work, based on the vacancy loops method described by Zepeda-Ruiz et al. [45], the initial dislocation densities in 36 samples with different sizes were precisely controlled in the range between $\sim 10^{15}$ m^{-2} and $\sim 10^{16}$ m^{-2}. By performing uniaxial compression simulations, we investigated the dislocation behaviors in pure Cu, random solid solution (RSS), and SRO CrCoNi SCPs, and probed the dislocation escape in CrCoNi SCPs having RSS and SRO. It is found that the critical pillar size required for having dislocation starvation in CrCoNi MEA SCPs is much smaller than that in pure metals. Most importantly, this work reveals the underlying reason for the retardation of mobile dislocation starvation in CrCoNi MEA SCPs.

2. Methods

MD simulations were carried out with the Large-scale Atomic/Molecular Massively Parallel Simulator (LAMMPS) [46]. Embedded atom method (EAM) interatomic potentials were used in this work. The EAM potential developed by Mishin et al. [47] has been widely used to explore the mechanical properties of various Cu systems, because of its reliable performance in reproducing important physical properties [48]. For the Cr-Co-Ni system, EAM interatomic potential developed by Li et al. [35] was adopted to compare the dislocation starvation behavior in RSS and SRO configurations under uniaxial compression.

The orientations of modeled nanopillars are $[1\bar{1}0]_x$, $[11\bar{2}]_y$, and $[111]_z$. Pure Cu SCPs were used to demonstrate the dislocation starvation behavior. Each model with a certain chemical SRO was subjected to a hybrid Monte Carlo (MC)/MD relaxation [49,50].

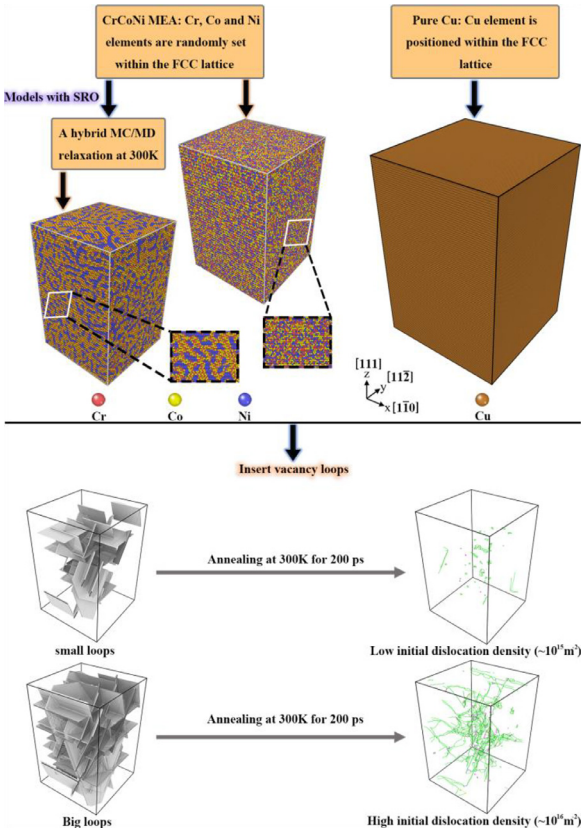

Fig. 1. A flowchart showing the modeling process of the SCPs.

A hybrid MC/MD relaxation with $N/4$ times (N is the number of atoms) of trial swaps every 0.05 ps for a total of 80000 MC cycles was performed based on an isobaric-isothermal (NPT) ensemble at 300 K and zero external pressure, to adequately relax each system. The parameters of chemical potential difference were set as $\Delta\mu_{Ni-Cr} = 0.32$ eV and $\Delta\mu_{Co-Cr} = 0.299$ eV. Firstly, the square-shaped perfect SCPs were made. Then, the vacancy loops method [45] was adopted to prepare the nanopillars with pre-existing dislocations. A total of 36 vacancy loops were introduced to the $(11\bar{1})$, $(1\bar{1}1)$, $(\bar{1}11)$, and (111) crystal planes by using the Atomsk package [51]. The SCPs were annealed at 300 K for 200 ps based on the NPT ensemble at zero pressure. If the initial dislocation density was not in the designated range, the sizes of the vacancy loops have to be adjusted, and annealed again, until the final structures meet the requirements. The initial dislocation density can be controlled by controlling the pre-existing vacancy loops, because subsequent dislocation interactions may prevent escapes of dislocations from the free surface. However, if the inserted vacancy loops were too small, especially when the dislocation density was lower than 10^{15} m^{-2}, it causes difficulty to control the dislocation density. Therefore, $\sim 10^{15}$ m^{-2} was defined as the lower bound for the initial dislocation density in our simulations. Fig. 1 shows the basic process for constructing the models.

To distinguish the CrCoNi MEAs with chemical SRO and RSS, planar distributions of elements are presented in Fig. 2(a, b). The line profiles of elemental concentrations for the SRO sample (Fig. 2(c)) fluctuate in the wide range from 46% to 13%. In contrast, the line profiles of elemental concentrations for the RSS sample (Fig. 2(d)) fluctuate moderately, suggesting the random distribution of elements. The SRO parameters for RSS and SRO samples are calculated based on the definition [52]:

$$\Delta p_{ij}^m = p_{ij}^m - p_{0.ij}^m \quad (1)$$

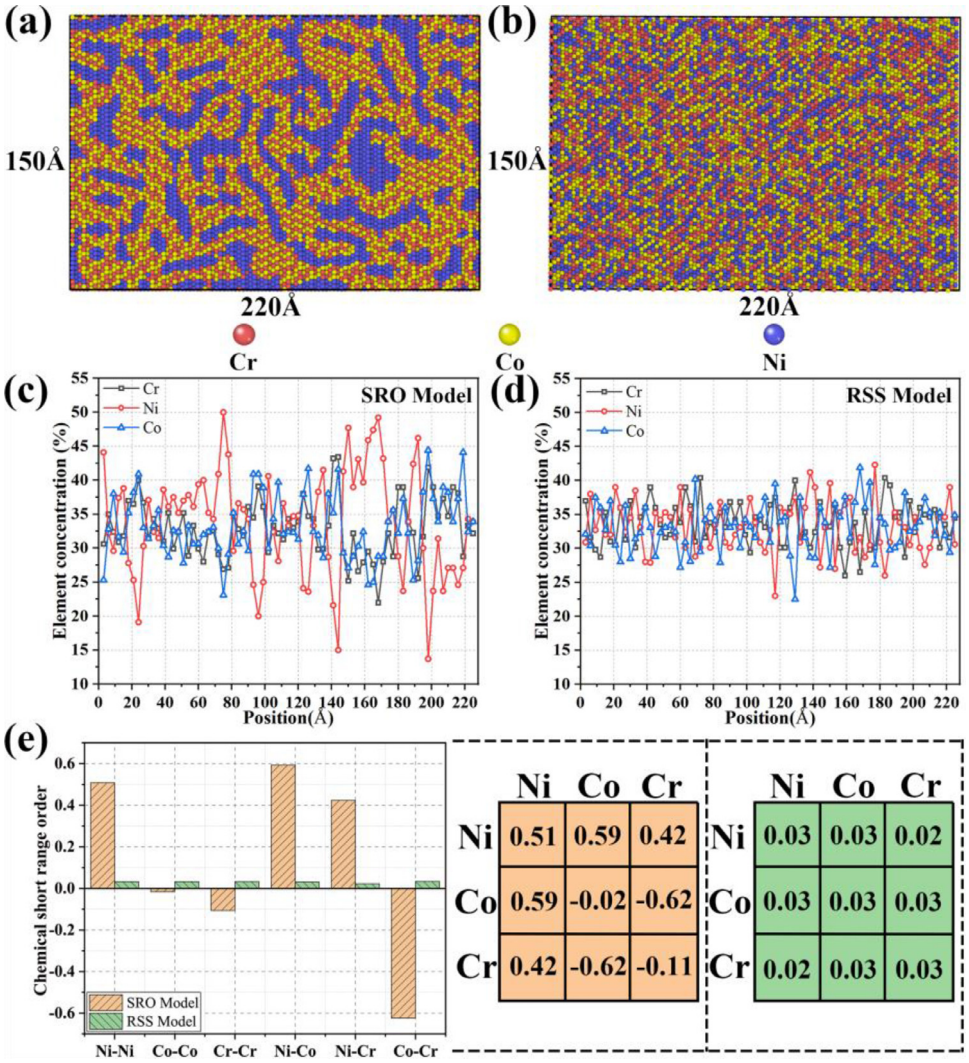

Fig. 2. (a, b) Atomic configurations for SRO and RSS CrCoNi systems, respectively. (c, d) Line profiles of elemental concentration taken from (a, b). (e) Chemical SRO parameters $\Delta\delta_{ij}^{1}$ for CrCoNi MEAs at 300 K.

where m is the mth nearest-neighbor shell of the central atom i, p_{ij}^{m} is the average probability of finding an atom of type j around the i-type atom within the mth shell, $p_{0,ij}^{m}$ is the average probability proportional to the corresponding concentration. The positive value of Δp_{ij}^{m} indicates the tendency of atom j approaching the mth shell of the atom i, while the negative value of Δp_{ij}^{m} indicates the opposite [35]. Fig. 2(e) shows that the SRO parameter for each pair of atoms in the RSS sample is close to zero, indicating the almost random distribution of three-principal elements. In contrast, the SRO parameters for SRO samples suggest an apparent ordering of elements. Note that the chemical SRO of various atomic pairs can be changed by different annealing times and temperatures in the experiments [33]. Therefore, our work only represents one case with high SRO.

Table 1 lists the dimensions and initial dislocation densities for the SCPs. The dislocation densities are set at $\sim 10^{15}$ m^{-2} and $\sim 10^{16}$ m^{-2}. Benzerga [53] pointed out that dislocation starvation occurs in single crystals with low dislocation densities. According to early experimental results, $\sim 10^{12}$ m^{-2} is considered low dislocation density, and $\sim 10^{15}$ m^{-2} is considered high dislocation density [54,55]. TEM is usually used to observe dislocations in thin samples including nano/micro-pillars but may underestimate the dislocation density because of the invisibility criterion for diffraction contrast imaging. However, the length of dislocations can be calculated accurately by the dislocation extraction algorithm (DXA) [56], thus the dislocation densities in simulations are higher than that measured by TEM.

All SCPs were energy-minimized using the conjugate gradient (CG) method with force and energy tolerances of 10^{-8} eV and 10^{-12} eV Å^{-1}, respectively. The time step of hybrid MC/MD relaxation was set to 2.5 fs. The other MD simulations were carried out with the time step of 5 fs. Compression simulations were performed by deforming the SCPs at a strain rate of 10^{8} s^{-1} under the canonical (NVT) ensemble, and the temperature was set to 300 K. Periodic boundary condition (PBC) was imposed parallel to the loading axis, while the planes perpendicular to the loading axis were considered free surfaces to minimize the effects of aspect ratio and boundary on the predicted compressive deformation behaviors [57]. The simulation results were analyzed with the Open Visualization Tool (OVITO) software [58].

3. Results

3.1. Uniaxial compression deformation of SCPs with low initial dislocation density

The compressive stress–strain curves for SCPs with different sizes are shown in Fig. 3(a, b, d, e, g, h). The pre-existing dislo-

Table 1
Dimension and the total initial dislocation densities for the <111> SCPs.

System	Sample	Pillar dimension (x nm × y nm × z nm)	High dislocation density (m^{-2})	Low dislocation density (m^{-2})
CrCoNi (RSS)	RSS-15-15-22.5	15 × 15 × 22.5	3.37×10^{16}	6.00×10^{15}
	RSS-20-20-30	20 × 20 × 30	3.28×10^{16}	3.68×10^{15}
	RSS-25-25-37.5	25 × 25 × 37.5	3.70×10^{16}	4.88×10^{15}
	RSS-30-30-45	30 × 30 × 45	3.78×10^{16}	3.49×10^{15}
	RSS-35-35-52.5	35 × 35 × 52.5	3.22×10^{16}	4.25×10^{15}
	RSS-40-40-60	40 × 40 × 60	3.33×10^{16}	4.22×10^{15}
CrCoNi (SRO)	SRO-15-15-22.5	15 × 15 × 22.5	3.44×10^{16}	3.70×10^{15}
	SRO-20-20-30	20 × 20 × 30	3.70×10^{16}	3.95×10^{15}
	SRO-25-25-37.5	25 × 25 × 37.5	3.64×10^{16}	3.74×10^{15}
	SRO-30-30-45	30 × 30 × 45	3.64×10^{16}	2.60×10^{15}
	SRO-35-35-52.5	35 × 35 × 52.5	3.20×10^{16}	5.65×10^{15}
	SRO-40-40-60	40 × 40 × 60	3.32×10^{16}	4.11×10^{15}
Cu	Cu-15-15-22.5	15 × 15 × 22.5	3.06×10^{16}	6.00×10^{15}
	Cu-20-20-30	20 × 20 × 30	3.55×10^{16}	4.04×10^{15}
	Cu-25-25-37.5	25 × 25 × 37.5	3.69×10^{16}	5.39×10^{15}
	Cu-30-30-45	30 × 30 × 45	3.54×10^{16}	4.89×10^{15}
	Cu-35-35-52.5	35 × 35 × 52.5	3.48×10^{16}	4.17×10^{15}
	Cu-40-40-60	40 × 40 × 60	3.25×10^{16}	4.29×10^{15}

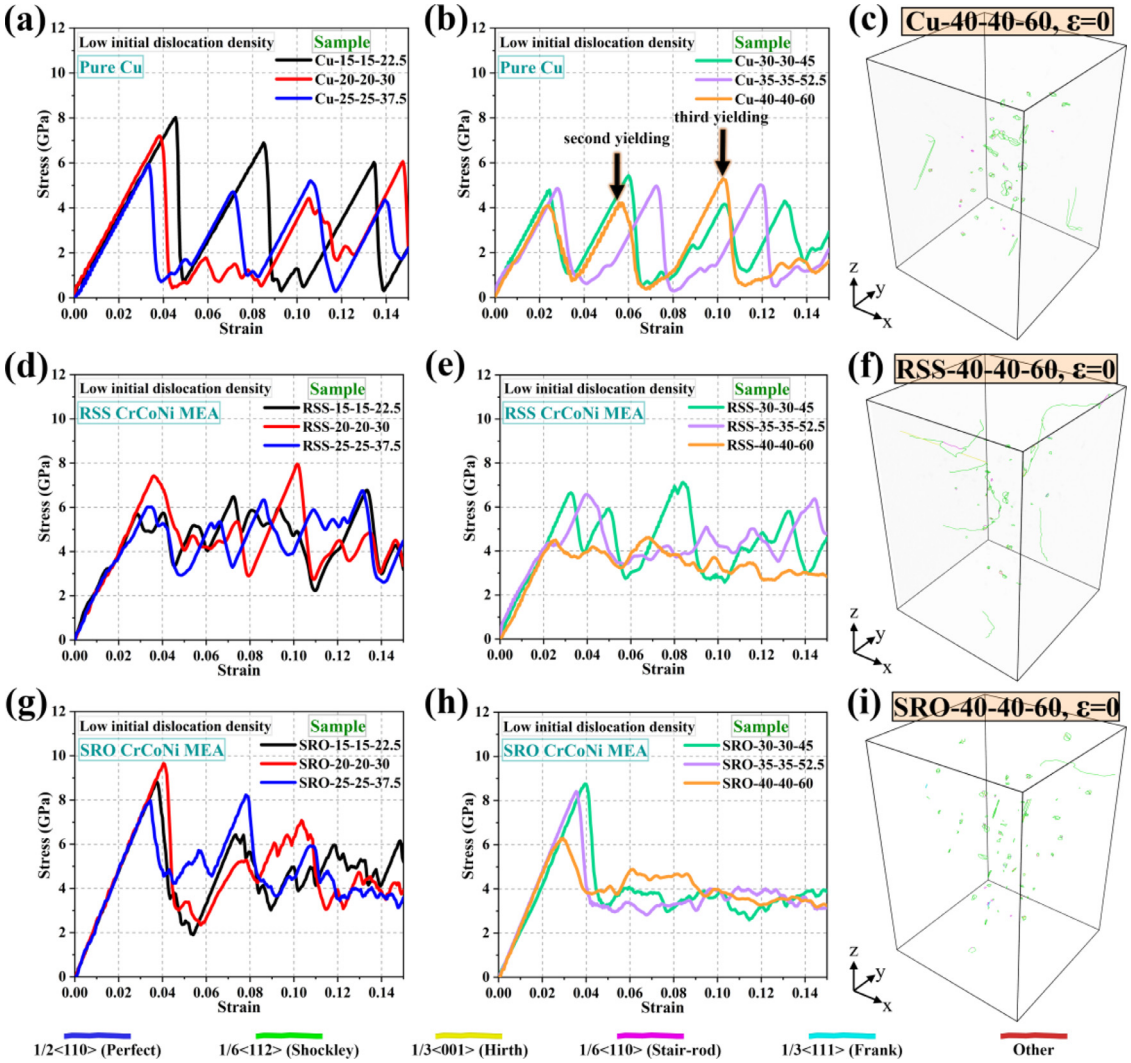

Fig. 3. Typical compressive stress–strain response of (a, b) Pure Cu, (d, e) RSS CrCoNi, and (g, h) SRO CrCoNi SCPs with low dislocation density (~10^{15} m^{-2}) and sizes ranging from 15 nm × 15 nm × 22.5 to 40 nm × 40 nm × 60 nm. (c, f, i) Initial dislocation distribution of 40 nm × 40 nm × 60 nm size SCPs corresponding to pure Cu, RSS, and SRO CrCoNi MEAs, respectively.

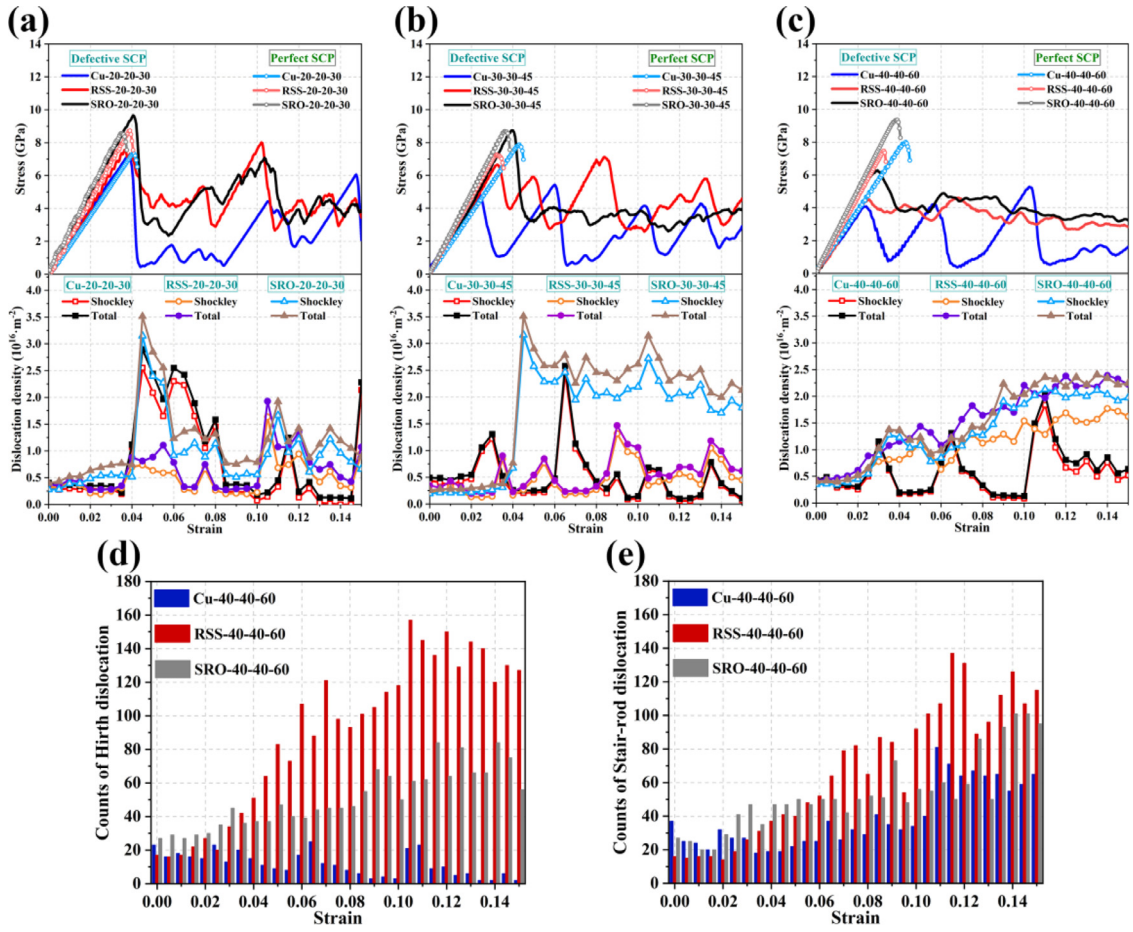

Fig. 4. Dislocation density vs strain plots under compressive loading for three kinds of SCPs with low dislocation density (~10^{15} m^{-2}). (a) 20 nm × 20 nm × 30 nm, (b) 30 nm × 30 nm × 45 nm, and (c) 40 nm × 40 nm × 60 nm. (d–f) Counts of Hirth and Stair-rod dislocations corresponding to the SCPs with different sizes.

cations were analyzed by DXA and shown in Fig. 3(c, f, i). After the first yielding of Cu SCPs, dislocation quickly escapes due to the influence of image force and the low probability of dislocation interaction at the nanoscale. However, there is no mobile dislocation inside for further plastic deformation (see Supplementary Videos S1 and S2), so the second and third yielding appear (see Fig. 3(b)). These intermittent re-yielding behaviors are also known as strain bursts or exhaustion hardening [59]. Interestingly, the stress–strain curves of RSS-30-30-45, RSS-35-35-52.5, and RSS-40-40-60 SCPs show a steady state of plastic flow (Fig. 3(e)). Furthermore, SRO CrCoNi SCPs do not show any significant strain bursts until the size dropped to 25 nm × 25 nm × 37.5 nm. Pure Cu, RSS, and SRO CrCoNi SCPs all show a significant trend of initial yield stress strengthening with decreasing pillar size, which is called "smaller is stronger" [13]. For example, the yield stress of the Cu, RSS, and SRO CrCoNi SCPs with a size of 40 nm × 40 nm × 60 nm is 4.09, 4.50, and 6.29 GPa, respectively. In contrast, the yield stress of these three SCPs with a size of 20 nm × 20 nm ×30 nm is 7.11, 7.31, and 9.66 GPa, respectively. However, the yield stress of perfect SCPs (see Fig. 4(a–c)) has no obvious size effect. This problem will be discussed in Section 4.2.

To explore the differences in dislocation behavior, the dislocation density of the SCPs with the size of 20 nm × 20 nm × 30 nm, 30 nm × 30 nm × 45, and 40 nm × 40 nm × 60 nm was adopted as examples, as shown in Fig. 4(a–c). Dislocation starvation (corresponding to the moment that the density of Shockley partial dislocation is close to zero) dominates the deformation process of SCPs with the size of 20 nm × 20 nm × 30 nm and 30 nm × 30 nm × 45 nm, except for the SRO-30-30-45 sample. It indicates that the deformation of relatively small CrCoNi SCP is also controlled by repeated dislocation avalanches. However, the SRO-30-30-45, SRO-40-40-60, and RSS-40-40-60 samples do not show dislocation starvation behavior. According to Ref. [60], dislocation pile-ups against dislocation bands were observed, resulting in intermittent and sectional movement of dislocations in $Al_{0.1}$CoCrFeNi HEA. While the deformation of the Cu pillar is dominated by a large number of frequently escaping dislocations. Similarly, our results indicate that the Cu-40-40-60 sample reaches a high dislocation density state (ρ_{total} = 2.72 × 10^{16} m^{-2}) after the third yielding (corresponding to $\varepsilon \approx 10\%$), but instead of retaining the dislocation network inside the pillar, almost all the mobile dislocations escape, as shown by the snapshots in Fig. 5(a). Fig. 5(b, c) shows the evolution of the dislocation network in the MEA SCPs under plastic deformation. RSS-40-40-60 is the sample with the most counts of Stair-rod and Hirth dislocations of all the SCPs with a size of 40 nm × 40 nm × 60 nm, as shown in Fig. 4(d, e). The visualization results matched with the statistical results also show that a large number of sessile Hirth and Stair-rod dislocations restrict the activity of mobile Shockley partial dislocations, as shown in Fig. 5(b). The dynamic deformation details of the relatively large RSS SCPs (Supplementary Video S4) intuitively reflect the constraint from sessile dislocations. Although the number of Stair-rod and Hirth dislocations in the SRO-40-40-60 sample is relatively small, its mobile Shockley partial dislocation density is significantly higher than that of the RSS-40-40-60 sample (Fig. 4(c)), and even induces obvious multiplication of mobile dislocations, as revealed in Fig. 5(c).

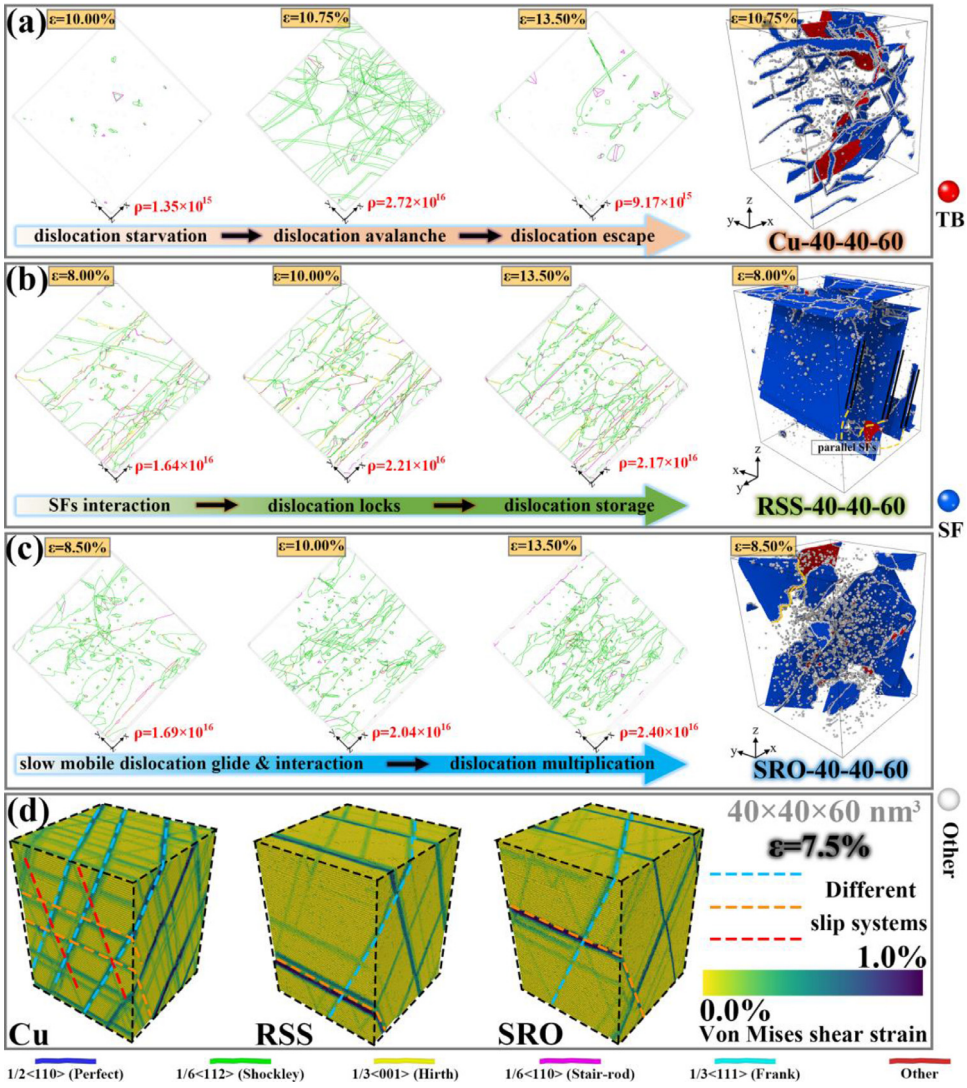

Fig. 5. Compression deformation behavior of SCPs with the size of 40 nm × 40 nm × 60 nm. Dislocation networks of (a) Cu-40-40-60, (b) RSS-40-40-60, and (c) SRO-40-40-60 SCPs at different strain. (d) Local von Mises shear strain of the three SCPs at $\varepsilon = 7.5\%$.

Current visualization technology cannot capture the escaping dislocations on a free surface. Therefore, here we qualitatively compare the degree of dislocation escape in the three kinds of SCPs, in accordance with von Mises effective strain. To obtain the local shear strain $\varepsilon_m^{\text{Mises}}$ for mth atom, a local transformation matrix P_{m} is determined by the expression [61]:

$$\boldsymbol{P}_{\text{m}} = \left(\sum_{n \in N_m^0} (\boldsymbol{l}_{mn}^0)^{\text{T}} \boldsymbol{l}_{mn}^0 \right)^{-1} \left(\sum_{n \in N_m^0} (\boldsymbol{l}_{mn}^0)^{\text{T}} \boldsymbol{l}_{mn} \right) \tag{2}$$

where $\boldsymbol{l}_{mn}^0$ and $\boldsymbol{l}_{mn}$ are row vector separations related to mth and nth atoms, and the superscript 0 represents the reference moment of $\varepsilon = 0\%$. N_m^0 is the total number of nearest neighbors of the mth atom. The local strain matrix ε_{m} for the mth atom is calculated by:

$$\varepsilon_{\text{m}} = \frac{1}{2}\left(\boldsymbol{P}_{\text{m}}\boldsymbol{P}_{\text{m}}^{\text{T}} - 1\right) \tag{3}$$

Then, the local shear strain can be calculated:

$$\varepsilon_{\text{m}}^{\text{Mises}} = \sqrt{\varepsilon_{xy}^2 + \varepsilon_{xz}^2 + \varepsilon_{yz}^2 + \frac{(\varepsilon_{xx} - \varepsilon_{yy})^2 + (\varepsilon_{xx} - \varepsilon_{zz})^2 + (\varepsilon_{yy} - \varepsilon_{zz})^2}{6}} \tag{4}$$

The dark color represents the atoms with the higher local shear strain, as shown in Fig. 5(d). The dotted lines in three different colors represent the traces of the dislocations escaping from the free surface. The densest and most visible traces are found in Cu-40-40-60 SCP, while only a few dark traces are shown in RSS-40-40-60 and SRO-40-40-60 SCPs, indicating that the dislocation escape behavior in MEA is weakened in MEA in comparison to pure metals. Besides, the dark traces of RSS-40-40-60 SCP are almost parallel, which corresponds to the parallel SFs in Fig. 5(c).

3.2. Uniaxial compression deformation of SCPs with high initial dislocation density

The stress–strain response of SCPs with initial dislocation densities of $\sim 10^{16}$ m^{-2} is shown in Fig. 6(a–f). The yield stresses are close to the experimental values of the submicron-sized SCPs (0.75-1.05 GPa for pure Cu [44] and 1.5–2.5 GPa for CrCoNi MEA [62,63]). Besides, pure Cu and two kinds of MEA SCPs reach the yielding state in advance ($\varepsilon_{\text{yield,Cu}} < 1\%$ and $\varepsilon_{\text{yield,CrCoNi}} < 2.5\%$), while the corresponding values of perfect SCPs or pillars with low initial dislocation density are significantly greater than 1% and 2.5% (see Fig. 4(a–c)). The stress–strain curves for Cu SCPs always show strain bursts after yielding, and the extents of strain bursts increase

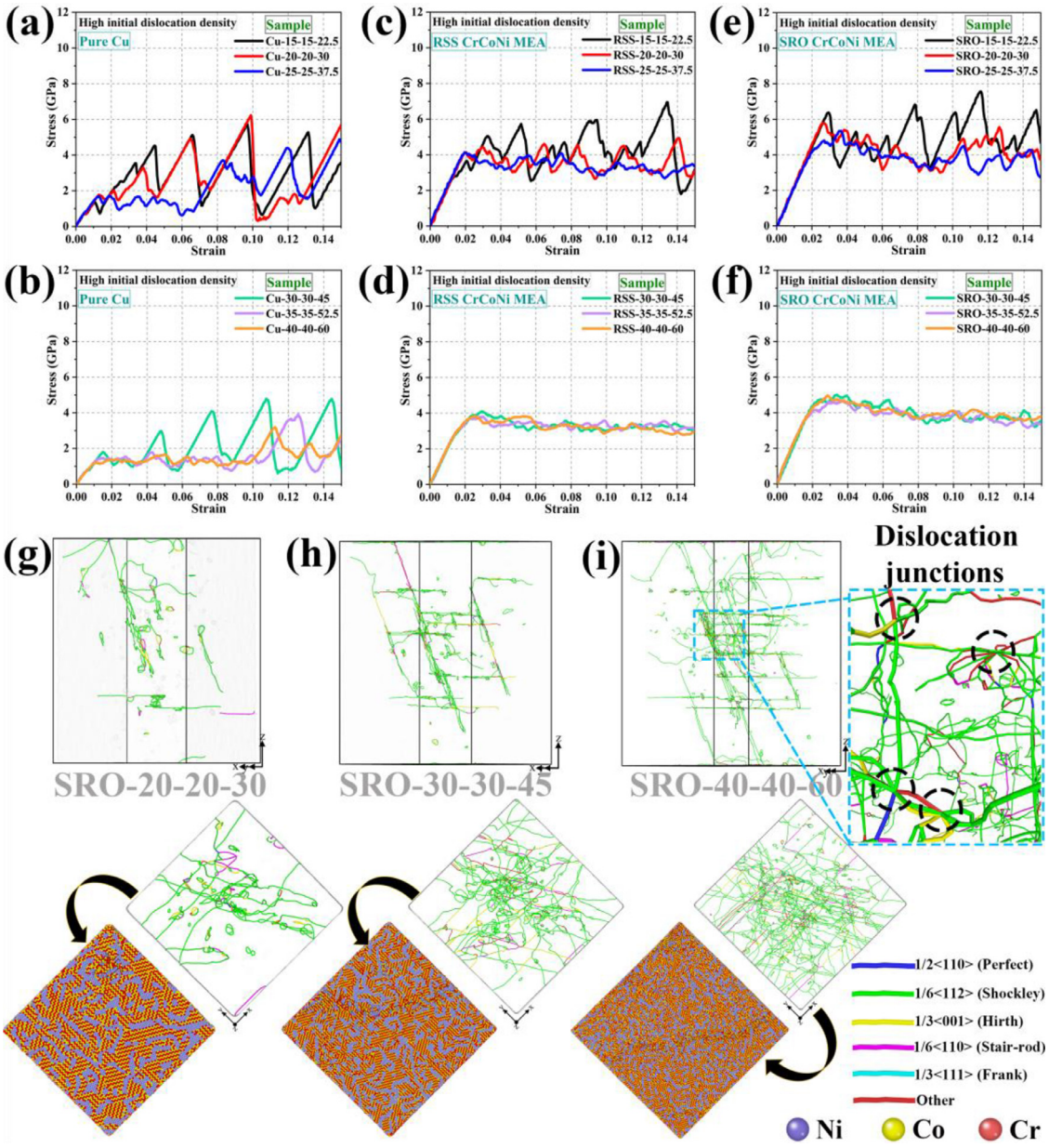

Fig. 6. Typical compressive stress-strain response of (a, b) Pure Cu, (c, d) RSS CrCoNi, and (e, f) SRO CrCoNi SCPs with high initial dislocation density ($\sim 10^{16}$ m^{-2}) and sizes ranging from 15 nm × 15 nm × 22.5 nm to 40 nm × 40 nm × 60 nm. Dislocation distribution of (g) SRO-20-20-30, (h) SRO-30-30-45, and (i) SRO-40-40-60 samples before yielding. Local enlargement in the blue dotted frame shows multiple dislocation junctions in a high initial dislocation density SCPs.

with the decrease of pillar size. For example, the Cu-35-35-52.5 and Cu-40-40-60 SCPs in Fig. 6(b) do not exhibit strain bursts until $\varepsilon > 10\%$. In contrast, the SCPs with a size smaller than 30 nm × 30 nm × 45 nm all exhibit at least three strain bursts during the deformation, as shown in Fig. 6(a, b). However, the stress–strain curves of RSS and SRO CrCoNi SCPs present a nearly consistent flat shape, and the strain bursts did not occur until the sample size is reduced to 25 nm × 25 nm× 37.5 nm. Besides, the amplitude of strain bursts is significantly smaller than that of the corresponding SCPs with low initial dislocation densities. Fig. 6(g–i) shows the dislocation distribution of SRO-20-20-30, SRO-30-30-45, and SRO-40-40-60 SCPs before yielding (other SCPs are shown in Supplement Material S2). The partially enlarged view of Fig. 6(i) shows the dislocation junctions of the associated multi-slip systems. The high-density dislocation network in the SCPs is a widespread dislocation source, it induces strong short-range interactions between dislocations at the beginning of deformation to slow down the dislocation escape. Correspondingly, the dislocation network evolution of the three typical SCPs containing high initial dislocation density is shown in Supplementary Videos S8–S10.

Fig. 7(a–c) shows the evolution of total dislocation density and Shockley partial dislocation densities vs strain. Although the dislocation exhaustion occurred in the SRO-20-20-30 SCP, the escape rate of mobile dislocation is low (from $\rho_{\text{shockley, }\varepsilon=0\%} = 3.70 \times 10^{16}$ m^{-2} to $\rho_{\text{shockley, }\varepsilon=15\%} = 7.78 \times 10^{15}$ m^{-2}), while the Shockley partial dislocations in Cu-20-20-30 SCP have been completely exhausted at $\varepsilon \approx 5\%$. On the contrary, for RSS-20-20-30 SCP, Shockley partial dislocations are stable, and dislocation escape is restricted (Fig. 7(a)) due to the presence of a number of sessile Hirth dislocations (Fig. 7(c)). As shown in Fig. 7(d), the dislocation density of Shockley of RSS-30-30-45 SCP does not decrease but continues to increase. SRO-30-30-45 SCP also maintains a stable dislocation density. When the pillar size is 40 nm × 40 nm × 60 nm (see Fig. 7(g)), the Shockley partial dislocation density of two CrCoNi

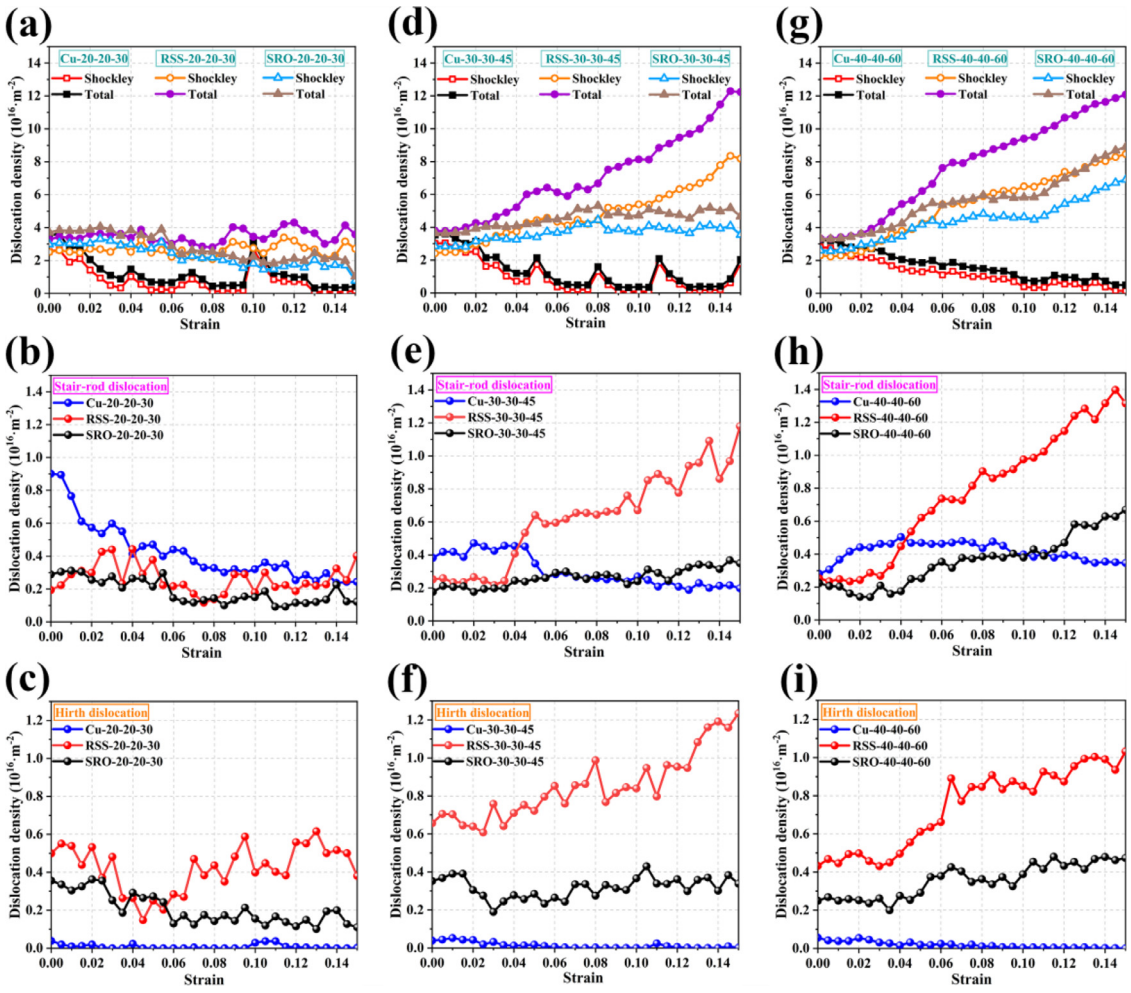

Fig. 7. Dislocation density plots under compressive loading for SCPs with high initial dislocation density (~10^{16} m^{-2}). (a, d, g) Total and Shockley partial dislocation density, (b, e, h) Stair-rod dislocation density, and (c, f, i) Hirth dislocation density.

SCPs keeps increasing during the plastic deformation. The statistical Stair-rod and Hirth dislocation density (see Fig. 7(b, c, e, f, h, i)) indicate that the multiplication of mobile dislocation in RSS and SRO SCPs may be related to the dislocation locks. For pure Cu, the trend of dislocation exhaustion cannot be well overcome even with high initial dislocation density and relatively large pillar size. To provide a more convincing case of this phenomenon in pure Cu, the Supplementary Material S3 shows that the dislocation starvation happens in the SCP with a size of 70 nm × 70 nm × 105 nm, which contains approximately 43 million atoms.

Calculating the densities of Stair-rod and Hirth dislocations alone has limitations in understanding the specific information of dislocations since it is not rigorous to equate all related types of dislocation to both lock structures (Lomer–Cottrell (L–C) and Hirth). Besides, L–C and Hirth dislocation locks are not really immobile because they may still disappear due to surface annihilation under high stress [64]. Based on the above considerations, the total numbers of these two kinds of dislocations and the length of single dislocation were counted when ε = 1%, 7.5%, and 15%, as shown in Fig. 8.

As shown in Fig. 8(a), pure Cu has the largest count of Stair-rod dislocations. However, Fig. 8(d) shows that nearly all length of the Stair-rod dislocations in Cu-40-40-60 is below 70 Å, except for the only longest Stair-rod dislocation. We notice that this longest Stair-rod dislocation is associated with the glissile junction (see Fig. 8(a)), which is a mobile structure associated with a pinning point, and it will move out of the free surface after yielding. The same junction was also found in RSS-40-40-60 SCP in Fig. 8(a). Besides, it is reasonable for RSS-40-40-60 SCP to have the maximum single dislocation length at ε = 1% since the low γ_{isf} of RSS CrCONi can induce a large number of intersecting SFs, which inevitably lead to many dislocation locks. For RSS-40-40-60 and SRO-40-40-60 SCPs, Hirth dislocation appears mostly as the dislocation locks (see the enlarged illustrations in Fig. 8(a, b)). However, all of the Hirth dislocations in Cu are not dislocation locks, since the count of Hirth dislocation in Cu (Fig. 8(a–c)) has a strong correlation with dislocation starvation (Fig. 8(d–f)). We found that these Hirth dislocations in Cu are actually generated during the cross-slip, while the cross-slip in SRO samples is mainly based on dislocation constriction (see Supplementary Material S4 for details). There is no mobile dislocation left in the Cu SCPs, but only the stable stacking fault tetrahedrons (SFTs) are retained at ε = 15% (see Fig. 8(c)). In contrast, there are a large number of mobile Shockley partial dislocations and L–C locks (the enlarged illustration in Fig. 8(c) shows L–C locks) in RSS-40-40-60 and SRO-40-40-60 SCPs, resulting in the high densities of dislocation networks. Although the initial single length of Stair-rod and Hirth dislocations in the SRO-40-40-60 is not as long as that of the RSS-40-40-60 (Fig. 8(d)), they maintain a more stable variation of length during the subsequent deformation process (Fig. 8(e, f)), which indirectly reflects that SRO samples slow down the dislocation reaction by inhibiting the movement of mobile dislocations. Therefore, strong chemical SRO is more con-

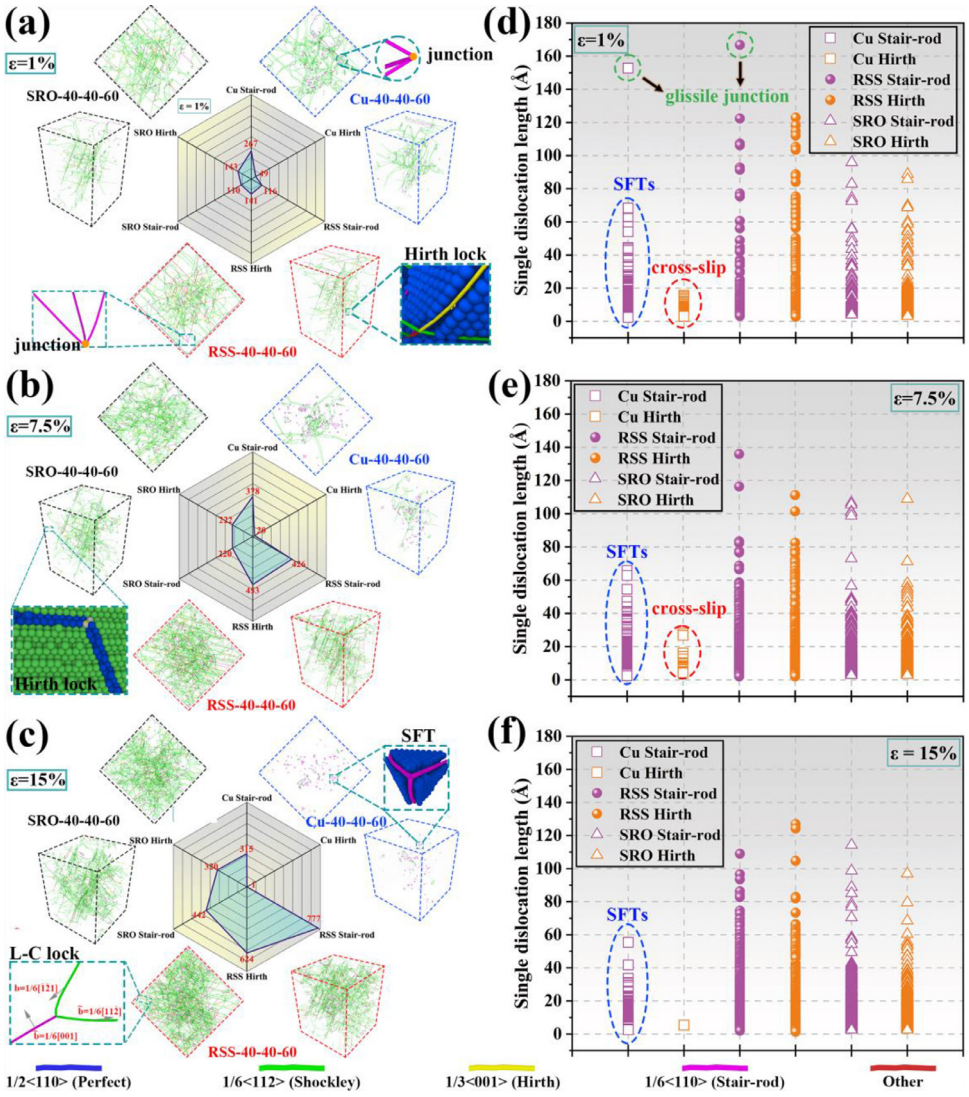

Fig. 8. DXA snapshot and counts of dislocations at different strains for SCPs with the dislocation density of ~10^{16} m^{-2}, where the blue, red, and black dotted lines contour represent Cu, RSS, and RSO CrCoNi SCPs, respectively. (a) ε = 1%, (b) ε = 7.5%, and (c) ε = 15%. Length of single dislocation at different strains for the SCPs with the size of 40 nm × 40 nm × 60 nm corresponding to (a, b, c). (d) ε = 1%, (e) ε = 7.5%, and (f) ε = 15%.

ducive to the stability of the dislocation network and the persistence of plastic deformation.

3.3. Hysteresis and discontinuity of dislocation glide

The long-range and short-range interactions between dislocations are unavoidable during the deformation of the SCPs, thus it is necessary to exclude these influences to compare the dislocation glide velocity of individual dislocation. A single crystal containing edge dislocation was constructed, as shown in Fig. 9(a). The *x*, *y*, and *z* axes are oriented along [110], [$\bar{1}$11], and [1$\bar{1}$2] directions, respectively. Here, in order to construct a periodic system, two crystals were merged along the y direction. One more layer of atoms was set along the *x*-direction of the upper crystal than that of the lower crystal and was compressed by 1/2 burgers vector ***b***, and the lower crystal was elongated by ***b***/2, so they both have the same length along the *x*-direction. Subsequently, after energy minimization and structural relaxation for a sufficiently long period of time, the dislocation velocity of Ni, Cu, and RSS/SRO MEAs was investigated by applying shear stresses at 300 K. Fig. 9(b, c) shows the dislocation structures in RSS and SRO models after relaxation. The configuration of edge dislocation exhibits fluctuations in atomic distance due to the random elemental distribution. In contrast, the initial configuration of edge dislocations in the SRO model shows large curvature, due to the large separation of Ni and Co-Cr atomic pairs. The Ni element exists in the form of nanoscale coherent precipitates, resulting in a fine distribution of ordered Co-Cr atomic pairs.

Fig. 10(a) represents the position of the edge dislocation as a function of simulation time. Here, the relationship between position and time was obtained by calculating the mean position of the leading and trailing partial dislocations over time, along the slip plane ($\bar{1}$11). The selected shear stresses were higher than the critical shear stress in each system to ensure the activation of the dislocation glide. As shown in Fig. 10(a), the ramp region represents the time interval for the applied shear stress to increase from zero to the target value, and the slope at each point of the curve equals the instantaneous dislocation velocity. By comparing the four position time function curves, it can be seen that pure Cu and Ni maintain almost the same dislocation velocity at almost every moment after the ramp region, because their corresponding curves almost coincide with the auxiliary straight lines. Similarly, Rodary et al. [65] applied shear stress slightly higher than the critical shear stress to the Ni-based alloy with extremely low Al concentration,

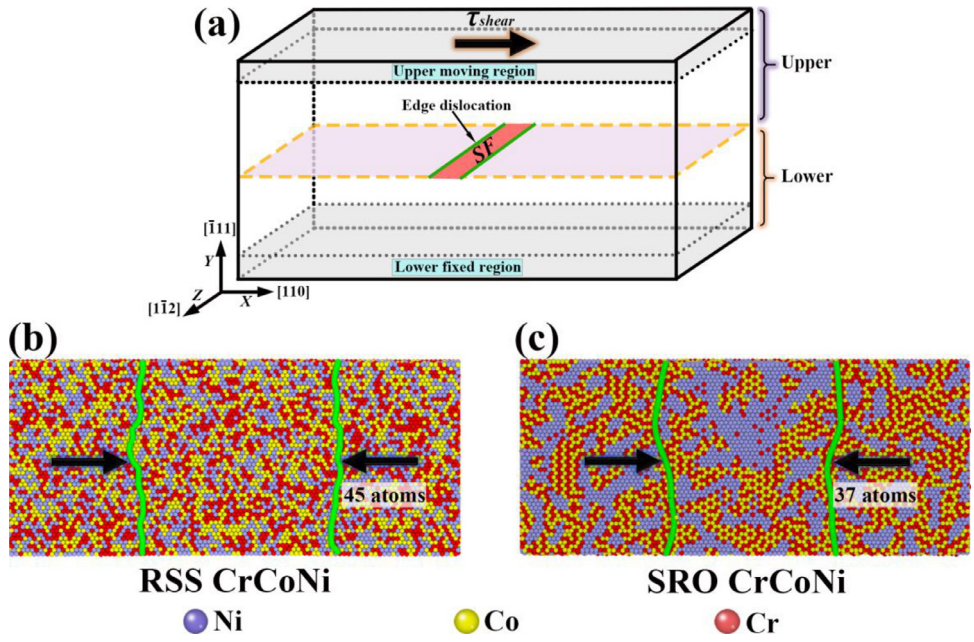

Fig. 9. (a) Schematic of the shear model in which the full edge dislocation spontaneously split into two Shockley partials linked by a stacking fault. Edge dislocation morphology after energy minimization and structural relaxation at 300 K: (b) RSS and (c) SRO CrCoNi models.

which also makes the edge dislocation glide at a constant velocity. Apparently, dislocations glide continuously in pure metals and traditional dilute solid solutions. However, the instantaneous dislocation glide velocities in RSS and SRO MEA samples change frequently during plastic deformation, evidenced by the nonlinearity of the position-time function, as shown in Fig. 10(a).

Fig. 10(b) shows the average dislocation velocity as a function of the applied shear stress. All curves demonstrate a nonlinear dislocation mobility relationship. Here a realistic exponential movement rule has been used to predict the dislocation mobility of pure metals below the first sound velocity [66,67]:

$$v = v_{\max}\left(1 - e^{-k\tau}\right) \tag{5}$$

where $v_{\max}$ is the value of the first sound velocity, k is a constant which is equal to 0.0146 MPa^{-1}. Apparently, Eq. (5) predicts the average dislocation velocities well for Ni and Cu, but not for CrCoNi MEAs. It is expected that lattice friction and chemical SRO will be taken into account in the mobility law in future investigations. With the increase of applied shear stress, the dislocation glide velocities of pure Cu and Ni reach the transonic speed. In contrast, the RSS and SRO CrCoNi samples do not reach the transonic speed even when the applied stress was as high as 1500 MPa. Interestingly, the shear stresses required to drive the edge dislocation glide in CrCoNi samples are significantly higher than that of the pure Ni and Cu. Besides, the calculated critical resolved shear stress of the SRO sample is about 500 MPa higher than that of the RSS sample, as shown in Fig. 10(b), explaining the fact that the yield stress and flow stress of SRO SCPs are all higher than those of the RSS ones. The snapshots in Fig. 10(c, d), show dislocation position and morphology from 30 to 52 ps. The dislocation lines in the pure Cu are nearly flat and moving fast. However, the dislocation lines are highly distorted and stayed still in the SRO CrCoNi MEA until 52 ps. Furthermore, in Supplementary Video S7, the shape of the edge dislocation lines in the CrCoNi sample keeps changing during the gliding process, indicating that the spatial heterogeneity of chemical composition contributes to the local pinning of the gliding dislocations.

3.4. Size dependence of dislocation exhaustion and multiplication

The relationship between the rate of dislocation exhaustion/multiplication and the sample size is shown in Fig. 11(a). For the sake of rigor, we performed three compression simulations on each sample (36 × 3 MD simulations in total), because slight atomic thermal oscillation may lead to inconsistent results. The rate of dislocation exhaustion was calculated as the ratio of mobile dislocation density to time until the first mobile dislocation starvation occurred.

The calculated discrete points show that the pure Cu, RSS, and SRO CrCoNi SCPs all exhibit power-law dependence on dislocation density evolution with different pillar sizes. Besides, whether at low or high initial dislocation densities, the trend of dislocation exhaustion in smaller-sized SCP ($\lesssim$ 20 nm) is significant, which is closely related to the annihilation of dislocations from the free surface. The influence of image force [67,68] cannot be ignored. Dislocation tends to approach the free surface to release its elastic strain energy. The image force F of the dislocation is related to the distance from the free surface l:

$$\frac{F}{L} = -\frac{Gb^2}{4\pi} \cdot \frac{1}{l} \tag{6}$$

$$\frac{F}{L} = -\frac{Gb^2}{4\pi(1-\nu)} \cdot \frac{1}{l} \tag{7}$$

the Eqs. (6) and (7) represent the image force acting on the screw and edge dislocations, respectively. Where L, G, b, and ν represent the length of the dislocation line, shear modulus, burgers vector, and Poisson's ratio, respectively. It can be seen that the image force depends on l^{-1}. Therefore, small-sized SCPs mean bigger image force, shorter effective free path of dislocation glide, and larger specific surface area (see Fig. 11(b)) of surface annihilation.

It is noteworthy that although the strain rate used in our work is commonly adopted in MD simulation due to the limitation of accessible length scales and timescales, such a high strain rate will lead to higher dislocation density than the real deformation process [66]. Thus, it is necessary to make a comparison with pure metals. The data in Fig. 11(a) illustrate that Cu SCPs do not reach

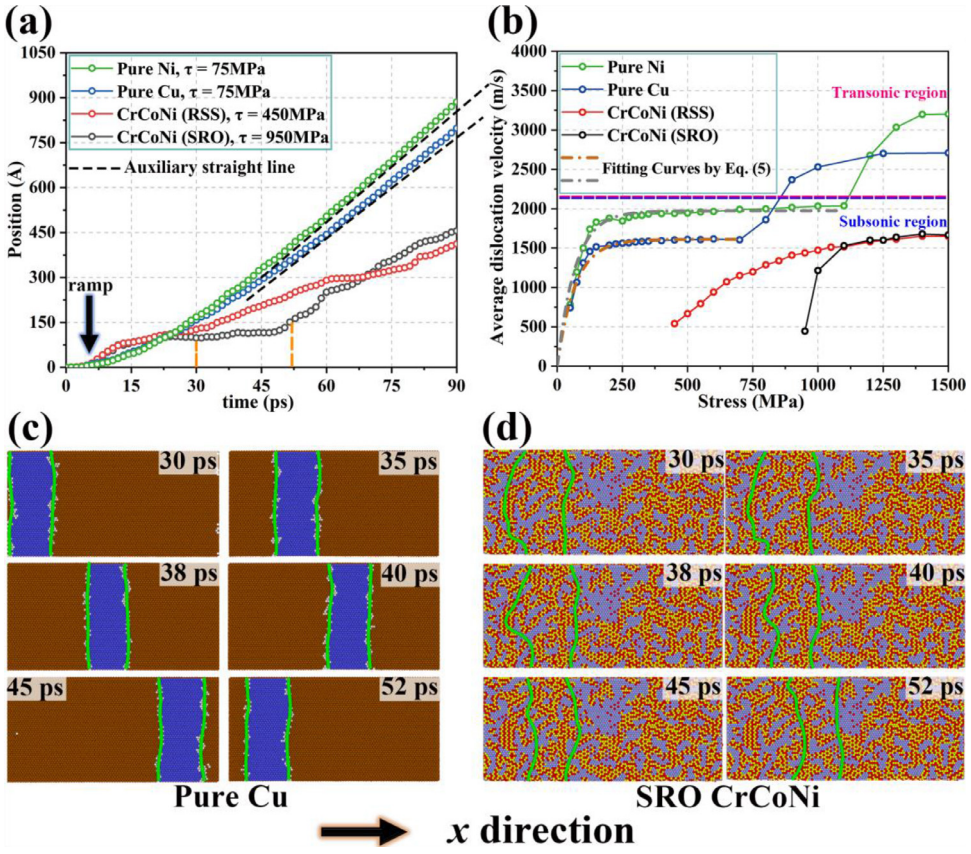

Fig. 10. (a) Time dependence of mean position for the edge dislocations in the SCPs at 300 K (the arrows indicate the ramp time interval). (b) Average dislocation velocity versus applied shear stress for edge dislocation. Snapshots showing the movement of an edge dislocation in (c) Pure Cu and (d) SRO CrCoNi. The green lines represent the contour of the edge dislocation.

the state of $r_e \approx r_m$ in any case. Moreover, the process of repeated dislocation starvation of Ni SCP with a size of 40 nm × 40 nm × 60 nm at the same strain rate is shown in Supplementary Material S5. Another convincing event comes from experiments that CrCoNi MEA SCPs show minor stress fluctuation even at the strain rate of 1×10^{-2} s^{-1} [63].

As shown in Fig. 11(c, d), the strain proportion of 36 SCPs experiencing mobile dislocation starvation was counted by repeating the MD simulation three times. This quantified dislocation starvation gives an exciting result that although the mobile dislocation starvation occurred in the SCPs with relatively small size, the CrCoNi SCPs experienced only about half the relevant strain of the Cu SCPs.

4. Discussion

4.1. Fluctuating energy landscape effect

The generalized stacking fault energy (GSFE) surfaces of pure Ni, Cu, and RSS CrCoNi MEA are shown in Fig. 12(a–c). O_1IO_2 is the region corresponding to dislocation dissociation on the close-packed plane of FCC structure. The point *I* corresponds to the position of the lowest energy and is also called γ_{isf}, which is closely related to the dislocation dissociation. Generally, the width of extended dislocation increases with decreasing γ_{isf}. Colliding of SFs on intersecting planes results in L–C locks, when $\gamma_{isf} \leq 40$ mJ m^{-2} [69], which is also the cause for the large number of Stair-rod dislocations in the RSS CrCoNi MEA. Fig. 12(d) represents the curve of SFE along O_1UI. For pure Cu and Ni, γ_{isf} and γ_{usf} are both invariant values, but not for RSS CrCoNi MEA. We constructed 40 RSS models to calculate the SFEs. The random distribution of chemical elements in RSS models leads to different results, and the final calculated γ_{isf} and γ_{usf} are shown in Fig. 12(c). Note that the calculated γ_{isf} is about −18 mJ m^{-2}, which is close to the value of −24 mJ m^{-2} calculated by density functional theory (DFT) [62]. Furthermore, the stable SFE ($\gamma_{isf} = 64$ mJ m^{-2}) of the SRO sample is significantly higher than that of the RSS sample, which is close to that of the pure Cu (45 mJ m^{-2}). In previous experimental studies [32,33,70], quantitative visualization of the SRO structure was established, and the results demonstrated the preference for Ni-Ni/Co-Cr SRO atomic pairs in the CrCoNi MEA. Here, it is reasonable that the γ_{isf} of the SRO sample calculated by MD is higher than that of the experiments [70] (about 30 mJ m^{-2}) because the ordering of atomic pairs can be controlled by adjusting the temperature of hybrid MC/MD simulations. To emphasize the effect of SRO on dislocation starvation, we chose the temperature which can realize the highest SRO during hybrid MC/MD simulations. Fisher [71] pointed out that dislocation glide needs to destroy short-range ordered atom pairs, while dissipates a certain amount of energy which is proportional to the magnitude of the glide, thereby resulting in the strengthening of the entire deformation process. Schön [72] regarded SRO strengthening as the “frictional hardening” effect, and caused the dislocation to be locally dragged during movement. Therefore, SRO causes the increase in dislocation-nucleation barrier, which corresponds to the increase in unstable SFE.

The influence of chemical heterogeneities on dislocation starvation can be explained by the local unstable SFE in pure Ni, Cu, RSS, and SRO CrCoNi MEAs, as shown in Fig. 13. The calculated values of local unstable SFE for pure Ni and Cu {111}<112> are 365 mJ m^{-2} and 158 mJ m^{-2}, as shown in Fig. 13(a, b). However, the local unstable SFE values for RSS and SRO CrCoNi MEAs exhibit significant fluctuation along the {111}<112> slip direction. To

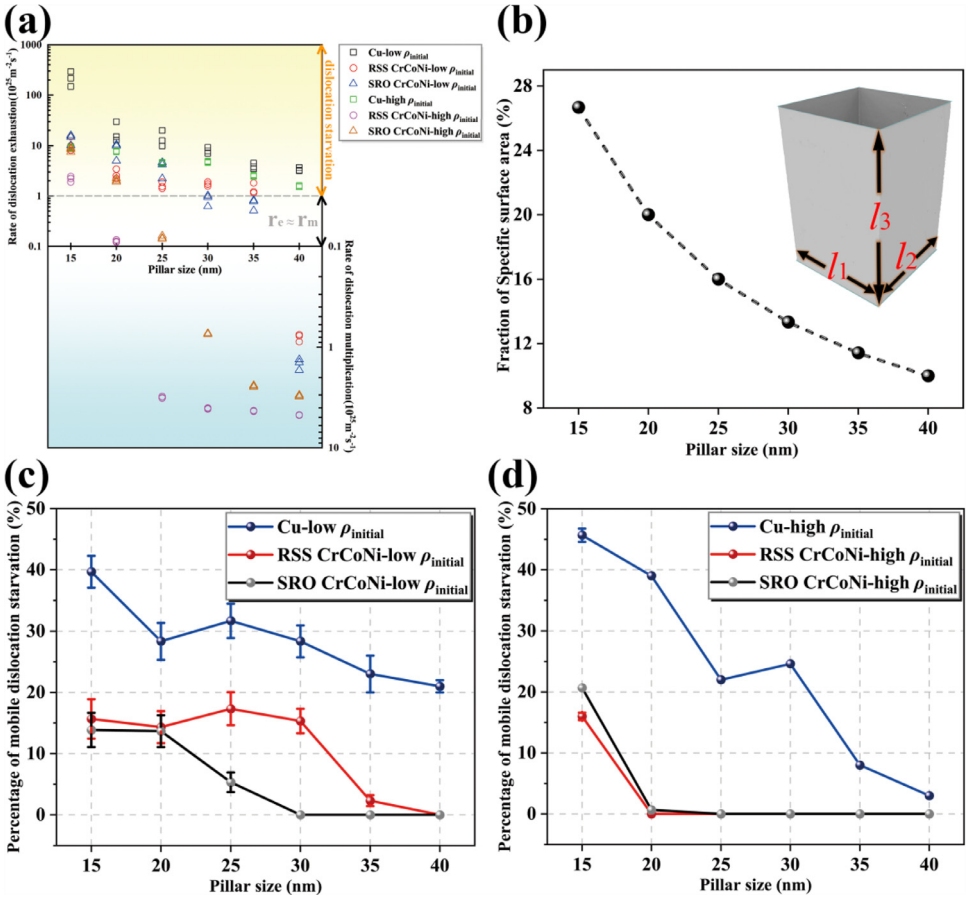

Fig. 11. (a) Rate of dislocation exhaustion and multiplication of Shockley partial dislocations for SCPs with different sizes under uniaxial compression. (b) Fraction of specific surface area, where the values are equal to $\frac{2[(l_1l_3)+(l_2l_3)]}{l_1l_2l_3}$ due to the application of free boundary conditions along the transverse direction. Total percentage of mobile dislocations during deformation vs pillar size for (c) low and (d) high initial dislocation density. For simplicity, the value of abscissa in the above four figures represents the side length of the square-shaped SCPs.

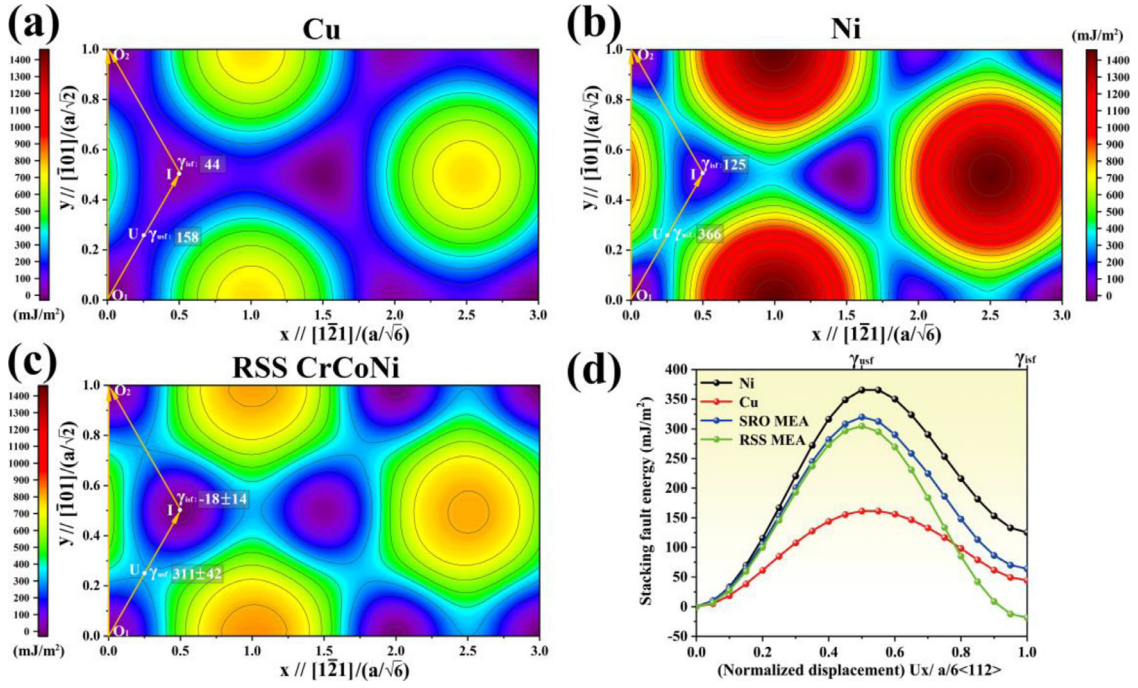

Fig. 12. Contour plots of the GSFE for (a) Cu, (b) Ni, and (c) RSS CrCoNi MEA. The unit length along the *x*-axis is $a/\sqrt{6}$ while the *y*-axis is $a/\sqrt{2}$, where *a* is the lattice constant. (d) Stacking fault energy curves corresponding to the path O_1-*U*-*I*. The unit length along the displacement direction is$a/\sqrt{6}$.

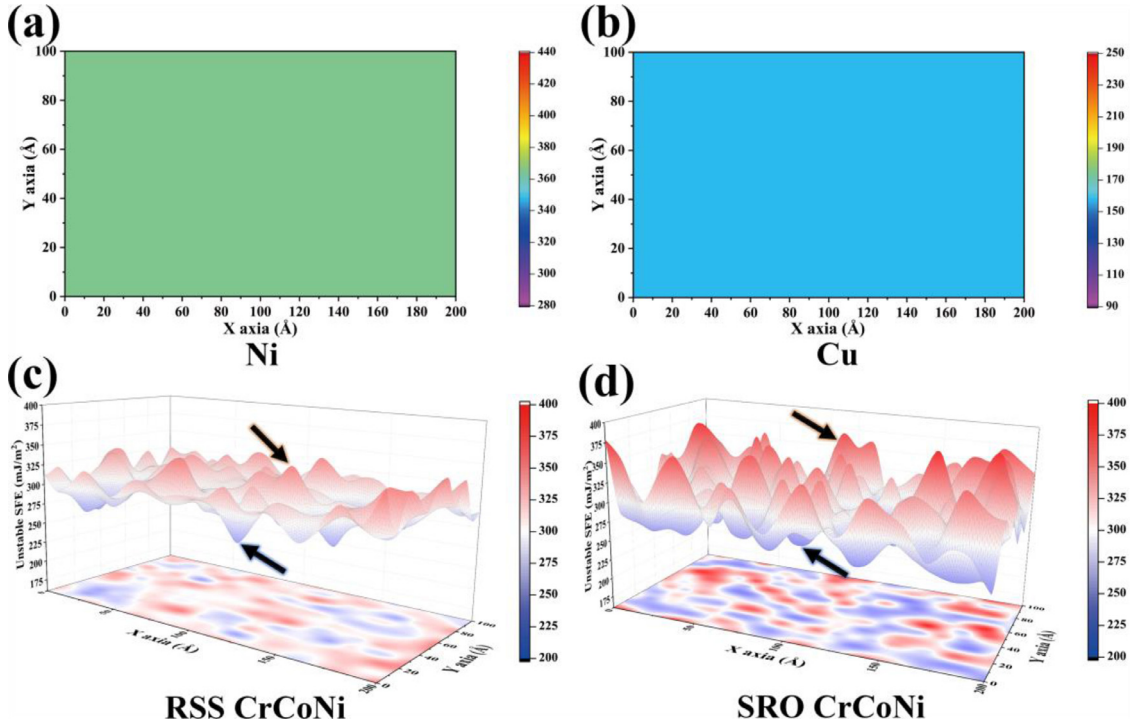

Fig. 13. (a, b) Local unstable SFEs distribution maps of Ni and Cu. (c, d) 3D mapping surface of local unstable SFEs for RSS and SRO CrCoNi MEAs.

highlight the differences between RSS and SRO samples, the three-dimensional contour plots of local unstable SFE were plotted, as shown in Fig. 13(c, d). The range of local unstable SFE values for RSS samples is 247–363 mJ m^{-2} (Fig. 13(c)), while that for SRO samples is 250–393 mJ m^{-2} (Fig. 13(d)). Strong spatial heterogeneity of local unstable SFE for CrCoNi MEAs indicates that the fluctuating energy barriers need to be overcome repeatedly. The dislocations will be hindered by high energy barriers (black arrow pointing to the lower right) and thus pile up at the region with low energy barriers (black arrow pointing to the upper left). To cross these peaks, sufficient driving force must be given continuously, otherwise, the dislocations will stagnate at the valley, which is in sharp contrast to the flat local unstable SFE planes for pure metals Ni and Cu. In particular, the fluctuant values of SRO CrCoNi MEA are more violently, which is the reason why SRO samples are less prone to dislocation exhaustion than RSS samples under the condition of low initial dislocation densities.

4.2. Initial dislocation density dependence of size effect

Submicron-sized and nano-sized pillars are usually fabricated from bulk material by FIB milling [15,73]. Nevertheless, the implantation of Ga^+ often induces vacancies and even altered dislocation density [74,75]. Thus, it is necessary to test a large number of samples for statistically reliable results. In our MD simulations, the initial dislocation density is carefully controlled for a better understanding of dislocation behaviors.

Numerous MD simulations have demonstrated dislocation nucleation from free surfaces [76] in perfect pillars, resulting in exaggerated yield stress in comparison to *in-situ* SEM compression test results [77]. The stress–strain responses of perfect SCPs are shown in Fig. 4(a–c). Since there are no relatively weak points on the free surface of perfect SCPs, the thermal vibration results in a random variation of yield stress within a small range. In contrast, the SCPs with pre-existing dislocations show significant yield stress differences, complying with the "smaller is stronger" effect [13]. This effect is caused by the activation of pre-existing dislocations inside the SCPs prior to dislocation nucleation from the free surface. For example, the initial yielding of the SRO-40-40-60 SCP in Supplementary Video S6 is related to the activation of pre-existing dislocations inside the pillar. However, the activation of pre-existing dislocations in the SRO-30-30-45 and SRO-35-35-52.5 SCPs occurs almost simultaneously with dislocation nucleation at the surface. According to Ref. [78], the single crystalline nanowires without pre-existing dislocations show yield stresses near the theoretical strength and no apparent size effect. In contrast, some single crystals without pre-existing dislocations may also demonstrate a size effect due to surface roughness [79] and specific sample geometries [80]. Therefore, for a perfect single crystal with well-controlled geometry and smooth surface in the MD simulation, the size effect is hardly operative.

"Smaller is stronger" effect occurs in the SCPs with low initial dislocation density, as shown in Fig. 3. However, the SCPs with high initial dislocation density show a weak size effect on yield stress only when the sample is smaller than 25 nm × 25 nm × 37.5 nm (Fig. 6(a–f)). In order to explain this phenomenon, we investigated the relationship between the maximum length of single dislocation and first yield stress. Fig. 14(a) reveals the inverse correlation between the maximum dislocation length and the yield stress of the SCPs with low initial dislocation density, which is qualitatively consistent with the previous results [81,82]. In this case, the Shockley partial dislocation, indicated by the arrow in Fig. 14(a), is the only pre-existing mobile dislocation that has activated in SRO-40-40-60 SCP (supplementary Video S6). In contrast, the inverse correlation is weakened in the pillars with high initial dislocation density, as shown in Fig. 14(b). Such a difference can be attributed to the dense dislocation network in the samples with high initial dislocation densities. The mobile dislocations on each slip system were restrained by multiple dislocation junctions, creating a high density of dislocation sources in SCPs for the dislocation-mediated plastic deformation. Therefore, a large number of pre-existing dislocations within the SCPs can be activated at low stress, and most of them are activated almost simultaneously, as shown in Supplementary Video S8. The above phenomena in-

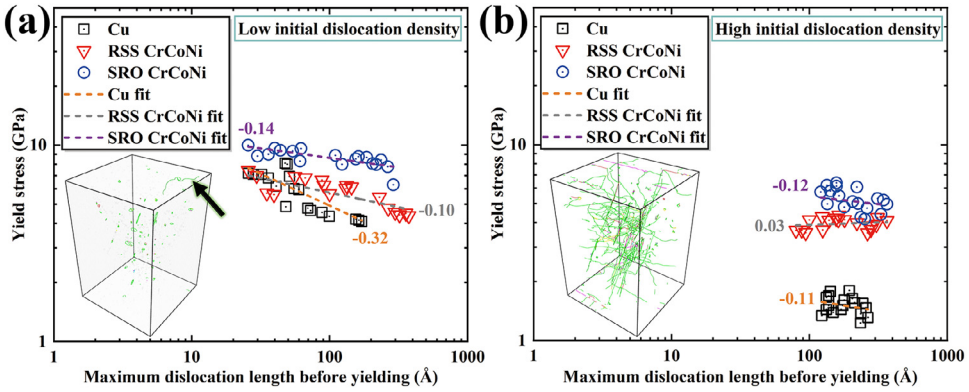

Fig. 14. Correlation between the maximum dislocation length and the yield stress for 3 × 36 samples. (a) SCPs with low initial dislocation density and (b) SCPs with high initial dislocation density. The illustrations show the dislocation network of a typical SCP before yielding.

dicate that the size effect is very sensitive to the number of available dislocation sources. The size effect has a significant correlation with the maximum length of single dislocation only when a small number of available sources exist.

According to our results, forest hardening is ineffective during the deformation of SCPs with high dislocation densities, such as the SRO-40-40-60 sample shown in Fig. 6(f). This is attributed to the inability of nano-scaled pillars to accommodate a large number of long dislocations and does not have sufficient volume for long-range and short-range interactions, hence forest hardening is disabled [83,84]. TEM observation [85] also suggests that the dislocation configurations and interactions inside a pillar sample are similar to that of bulk metals only when the pillar size is larger than about 1000 nm.

4.3. Dislocation starvation in pure metal and multi-element alloys

Although all the pillars with a size of 20 nm × 20 nm × 30 nm experience a mobile dislocation starvation state, as shown in Fig. 4(a), the lowest dislocation density of SRO and RSS SCPs is still higher than that of Cu. As shown in Supplementary Material S1 and Supplementary Videos S1, S3, and S5, dislocation loops and tangled dislocations inside the SRO-20-20-30 and RSS-20-20-30 SCPs are rarely eliminated during the multiple strain bursts. In contrast, the pre-existing dislocation loops and tangled dislocations tend to overflow the free surface during the dislocation avalanche process of the Cu-20-20-30 sample. The tardive movement of dislocations in MPEAs makes it possible to observe the dynamics of dislocation activities in TEM and SEM [60], but in contrast, the extremely fast dislocation escape in pure metals has to be captured by MD simulation in detail. Numerous studies have previously reported the deformation behavior of submicron-sized pure metal SCPs, such as pure Al [86], Cu [42,44], Au [87], and Ag [88]. The deformation processes of these pure metals are all dominated by the dislocation starvation mechanism, which is closely linked to the strain bursts and intermittent surface nucleation and annihilation of dislocations. This phenomenon is re-confirmed by our MD simulation on the deformation behaviors of pure Cu SCPs, as shown in Figs. 4 and 7. In pure metals, Shockley partial dislocations escape rapidly (Fig. 11(a)) due to the negligible Peierls–Nabarro barriers. Meanwhile, nucleation and annihilation of dislocations occurred frequently and vigorously. According to Fu et al. [89], the AuCu nanowires with a diameter of 16 nm exhibit super plasticity tensile deformation attributed to the dynamic equilibrium of dislocation densities. The dislocation densities in the AuCu nanowires were also maintained at ~2.8×10^{16} m^{-2}, which is consistent with the dislocation density in our simulations as demonstrated in Figs. 4(b) and 7(a). The *in-situ* compression tests of Cu-15 at.%Al nano-sized SCPs also showed that the strain bursts are narrower and smaller than that of pure Cu [15], which indirectly suggests that the addition of alloying elements does slow down the dislocation exhaustion rate of small-sized SCPs. However, in such dilute solid solutions, dislocation starvation still occurs on a scale of submicron [15]. Therefore, we suggest that the alloys of concentrated solid solutions are promising to reduce the critical sample size for dislocation starvation. Nevertheless, there are many other factors that can affect the dislocation exhaustion process of SCPs, such as the degree of lattice distortion and pillar shape, which are worth further exploration.

Our simulation results for the SRO-40-40-60 SCP with low initial dislocation density indicate that the reduction of the stacking fault width due to the high γ_{isf} leads to a low probability of dislocation locks (Fig. 12(d)). Although the extended dislocations are rarely restricted by dislocation locks in this case, SRO can effectively prevent dislocation starvation. Strong SRO not only elevates the critical shear stresses for driving leading partials (Fig. 10(b)), but also induces violent fluctuations of energy barriers (Fig. 13(d)), which makes the nucleation and glide of dislocations more difficult. Therefore, the pillar size must be reduced to obtain a higher image force to eliminate extended dislocation. Commonly, dislocation locks act as obstacles to gliding dislocations, thereby promoting dislocation accumulation in bulk materials [34]. However, dislocation locks in the small-sized pure metal single crystals are not stable. Cui et al. [90] found that L–C locks in pure metal submicron-sized pillars are all destroyed or annihilated at the surface during cyclic loading, and finally lead to the exhaustion of mobile dislocations. On the contrary, in our MD simulations, the sessile dislocations in the RSS/SRO CrCoNi SCPs are not broken but stabilize the gliding dislocations (Fig. 7(b, c, e, f, h, i)). Thus, this suggests conducting a detailed study of size-dependent dislocation locks stability in MPEAs pillar with low SFE by discrete dislocation dynamics simulations.

5. Conclusions

In summary, we have systematically investigated the dislocation escape behaviors of CrCoNi MEA SCPs under uniaxial compression by atomistic simulations and compared them with pure metals. The quantitative introduction of pre-existing dislocation sources is important for the realization of the size effect, which facilitates the comparison of MD simulations with the real samples. The key findings are summarized as follows:

(1) Chemical diversity is the crucial factor affecting dislocation glide in CrCoNi MEAs. For the SCPs with low initial dislocation density (~10^{15} m^{-2}), the excellent dislocation storage ability of

the CrCoNi SCPs is mainly due to the requirement of overcoming discrepant energy barriers during the dislocation glide.

(2) The SRO SCPs with low initial dislocation density ($\sim10^{15}$ m^{-2}) show better dislocation storage and multiplication abilities than RSS ones since the strong spatial heterogeneity of chemical composition causes more violent fluctuation of energy barriers at the nanoscale. The critical size of the SRO CrCoNi SCPs for mobile dislocation starvation is about 10 nm lower than that of the RSS ones.

(3) The deformation of SCPs with high initial dislocation density ($\sim10^{16}$ m^{-2}) shows that the large number of pre-existing dislocation locks caused by negative stable SFEs of RSS CrCoNi is the main reason for more pronounced dislocation multiplication than that of SRO ones. Nevertheless, the critical size for the SCPs to reach dislocation starvation is ~15 nm due to the high density of pre-existing dislocation networks.

(4) The intermittent strain burst (exhaustion hardening) occurs in all investigated Cu SCPs with low ($\sim10^{15}$ m^{-2}) and high ($\sim10^{16}$ m^{-2}) initial dislocation densities. Importantly, the flat energy barriers of pure metals are the fundamental reason for the dislocation starvation.

Our results suggest that enhancing the chemical SRO in a nano-sized MPEAs SCP can prevent dislocation starvation, even if the initial dislocation density is very low. However, it should be noted that dislocation starvation is still the core mechanism dominating the deformation of nano-scaled MPEAs SCPs when the pillar size is less than a critical size due to the increased surface image force. Our discoveries are expected to be extended to other FCC MEA/HEAs due to the spatial heterogeneity of nanoscale chemical components.

Declaration of Competing Interest

The authors declare no conflict of interests.

CRediT authorship contribution statement

Luling Wang: Investigation, Methodology, Validation, Visualization, Software, Writing – original draft, Writing – review & editing. **Bin Liu:** Investigation, Writing – review & editing. **Jianqiu Zhou:** Funding acquisition, Project administration, Supervision. **Yang Cao:** Conceptualization, Funding acquisition, Writing – review & editing. **Feng Zhang:** Funding acquisition, Writing – review & editing. **Yonghao Zhao:** Investigation, Methodology, Funding acquisition, Writing – review & editing, Project administration, Supervision.

Acknowledgements

This work was financially supported by the Key University Science Research Project of Jiangsu Province (No. 17KJA130002), the Natural Science Foundation of Jiangsu Province (No. BK20201031), the National Key R&D Program of China (Grant No. 2021YFA1200203), and the National Natural Science Foundation of China (Grant Nos. 51971112 and 52071181).

Supplementary materials

Supplementary material associated with this article can be found, in the online version, at doi:10.1016/j.jmst.2022.07.065.

References

[1] M.D. Uchic, D.M. Dimiduk, J.N. Florando, W.D. Nix, Science 305 (2004) 986–989.
[2] C.A. Volkert, E.T. Lilleodden, Philos. Mag. 86 (2006) 5567–5579.
[3] L.B. Fu, D.L. Kong, C.P. Yang, J. Teng, Y. Lu, Y.Z. Guo, G. Yang, X. Yan, P. Liu, M.W. Chen, Z. Zhang, L.H. Wang, X.D. Han, J. Mater. Sci. Technol. 101 (2022) 95–106.
[4] D.L. Kong, T.J. Xin, S.D. Sun, Y. Lu, X.Y. Shu, H.B. Long, Y.H. Chen, J. Teng, Z. Zhang, L.H. Wang, X.D. Han, Nano Lett. 19 (2019) 292–298.
[5] L.H. Wang, K. Du, C.P. Yang, J. Teng, L.B. Fu, Y.Z. Guo, Z. Zhang, X.D. Han, Nat. Commun. 11 (2020) 1167.
[6] S.D. Sun, D.W. Li, C.P. Yang, L.B. Fu, D.L. Kong, Y. Lu, Y.Z. Guo, D.M. Liu, P.F. Guan, Z. Zhang, J.H. Chen, W.Q. Ming, L.H. Wang, X.D. Han, Phys. Rev. Lett. 128 (2022) 015701.
[7] D.M. Dimiduk, M.D. Uchic, T.A. Parthasarathy, Acta Mater. 53 (2005) 4065–4077.
[8] J.R. Greer, W.D. Nix, Phys. Rev. B 73 (2006) 245410.
[9] H. Tang, K.W. Schwarz, H.D. Espinosa, Acta Mater. 55 (2007) 1607–1616.
[10] J.R. Greer, W.C. Oliver, W.D. Nix, Acta Mater. 53 (2005) 1821–1830.
[11] W.D. Nix, J.R. Greer, G. Feng, E.T. Lilleodden, Thin Solid Films 515 (2007) 3152–3157.
[12] Z.W. Shan, R.K. Mishra, S.A. Syed Asif, O.L. Warren, A.M. Minor, Nat. Mater. 7 (2008) 115–119.
[13] S.H. Oh, M. Legros, D. Kiener, G. Dehm, Nat. Mater. 8 (2009) 95–100.
[14] W.D. Nix, S.W. Lee, Philos. Mag. 91 (2011) 1084–1096.
[15] R.M. Niu, X.H. An, L.L. Li, Z.F. Zhang, Y.W. Mai, X.Z. Liao, Acta Mater. 223 (2022) 117460.
[16] J.W. Yeh, S.K. Chen, S.J. Lin, J.Y. Gan, T.S. Chin, T.T. Shun, C.H. Tsau, S.Y. Chang, Adv. Eng. Mater. 6 (2004) 299–303.
[17] B. Cantor, I.T.H. Chang, P. Knight, A.J.B. Vincent, Mater. Sci. Eng. A 375–377 (2004) 213–218.
[18] M.H. Tsai, C.W. Wang, C.W. Tsai, W.J. Shen, J.W. Yeh, J.Y. Gan, W.W. Wu, J. Electrochem. Soc. 158 (2011) H1161.
[19] J.M. Zhu, H.M. Fu, H.F. Zhang, A.M. Wang, H. Li, Z.Q. Hu, Mater. Sci. Eng. A 527 (2010) 7210–7214.
[20] L.L. Xiao, Z.Q. Zheng, S.W. Guo, P. Huang, F. Wang, Mater. Des. 194 (2020) 108895.
[21] Z. Tang, T. Yuan, C.W. Tsai, J.W. Yeh, C.D. Lundin, P.K. Liaw, Acta Mater. 99 (2015) 247–258.
[22] M.H. Chuang, M.H. Tsai, W.R. Wang, S.J. Lin, J.W. Yeh, Acta Mater. 59 (2011) 6308–6317.
[23] B. Gludovatz, A. Hohenwarter, K.V.S. Thurston, H. Bei, Z. Wu, E.P. George, R.O. Ritchie, Nat. Commun. 7 (2016) 10602.
[24] J. Li, H.T. Chen, Q.H. Fang, C. Jiang, Y. Liu, P.K. Liaw, Int. J. Plast. 133 (2020) 102819.
[25] C. Varvenne, A. Luque, W.A. Curtin, Acta Mater. 118 (2016) 164–176.
[26] J. Li, Y. Chen, Q.F. He, X.D. Xu, H. Wang, C. Jiang, B. Liu, Q.H. Fang, Y. Liu, Y. Yang, P.K. Liaw, C.T. Liu, Proc. Natl. Acad. Sci. USA 119 (2022) e2200607119.
[27] Q. Yang, Y. Hu, J.M. Zuo, J. Mater. Sci. Technol. 95 (2021) 136–144.
[28] A.M. Giwa, Z.H. Aitken, P.K. Liaw, Y.W. Zhang, J.R. Greer, Mater. Des. 191 (2020) 108611.
[29] X. Ni, S. Papanikolaou, G. Vajente, R.X. Adhikari, J.R. Greer, Phys. Rev. Lett. 118 (2017) 155501.
[30] S. Maiti, W. Steurer, Acta Mater. 106 (2016) 87–97.
[31] L.T.W. Smith, Y.Q. Su, S.Z. Xu, A. Hunter, I.J. Beyerlein, Int. J. Plast. 134 (2020) 102850.
[32] X.F. Chen, Q. Wang, Z.Y. Cheng, M.L. Zhu, H. Zhou, P. Jiang, L.L. Zhou, Q.Q. Xue, F.P. Yuan, J. Zhu, X.L. Wu, E. Ma, Nature 592 (2021) 712–716.
[33] L.L. Zhou, Q. Wang, J. Wang, X.F. Chen, P. Jiang, H. Zhou, F.P. Yuan, X.L. Wu, Z.Y. Cheng, E. Ma, Acta Mater. 224 (2022) 117490.
[34] H. Li, H.X. Zong, S.Z. Li, S.B. Jin, Y. Chen, M.J. Cabral, B. Chen, Q.W. Huang, Y. Chen, Y. Ren, K.Y. Yu, S. Han, X.D. Ding, G. Sha, J.S. Lian, X.Z. Liao, E. Ma, J. Sun, Nature 604 (2022) 273–279.
[35] Q.J. Li, H. Sheng, E. Ma, Nat. Commun. 10 (2019) 3563.
[36] X.F. Yang, Y.Z. Xi, C.Y. He, H. Chen, X.C. Zhang, S.T. Tu, Scr. Mater. 209 (2022) 114364.
[37] C.J. Wang, B.N. Yao, Z.R. Liu, X.F. Kong, D. Legut, R.F. Zhang, Y. Deng, Int. J. Plast. 131 (2020) 102725.
[38] L.H. Wang, Y. Zhang, Z. Zeng, H. Zhou, J. He, P. Liu, M.W. Chen, J. Han, D.J. Srolovitz, J. Teng, Y.Z. Guo, G. Yang, D.L. Kong, E. Ma, Y.L. Hu, B.C. Yin, X.X. Huang, Z. Zhang, T. Zhu, X.D. Han, Science 375 (2022) 1261–1265.
[39] Q.Z. Li, L.H. Wang, J. Teng, X.L. Pang, X.D. Han, J. Zou, Scr. Mater. 180 (2020) 97–102.
[40] J. Li, B.B. Xie, Q.F. He, B. Liu, X. Zeng, P.K. Liaw, Q.H. Fang, Y. Yang, Y. Liu, J. Mater. Sci. Technol. 120 (2022) 99–107.
[41] P.S. Branício, J.P. Rino, Phys. Rev. B 62 (2000) 16950–16955.
[42] P. Rohith, G. Sainath, V.S. Srinivasan, Physica B 561 (2019) 136–140.
[43] M. Bagheripoor, R. Klassen, Mater. Sci. Technol. 36 (2020) 1829–1850.
[44] A.T. Jennings, M.J. Burek, J.R. Greer, Phys. Rev. Lett. 104 (2010) 135503.
[45] L.A. Zepeda-Ruiz, A. Stukowski, T. Oppelstrup, V.V. Bulatov, Nature 550 (2017) 492–495.
[46] S. Plimpton, J. Comput. Phys. 117 (1995) 1–19.
[47] Y. Mishin, M.J. Mehl, D.A. Papaconstantopoulos, A.F. Voter, J.D. Kress, Phys. Rev. B 63 (2001) 224106.
[48] C.B. Carter, I.L.F. Ray, Philos. Mag. 35 (1977) 189–200.
[49] B. Sadigh, P. Erhart, A. Stukowski, A. Caro, E. Martinez, L. Zepeda-Ruiz, Phys. Rev. B 85 (2012) 184203.
[50] B. Sadigh, P. Erhart, Phys. Rev. B 86 (2012) 134204.

[51] P. Hirel, Comput. Phys. Commun. 197 (2015) 212–219.
[52] J. Ding, Q. Yu, M. Asta, R.O. Ritchie, Proc. Natl. Acad. Sci. USA 115 (2018) 8919–8924.
[53] A.A. Benzerga, J. Mech. Phys. Solids 57 (2009) 1459–1469.
[54] S. Ni, Y.B. Wang, X.Z. Liao, S.N. Alhajeri, H.Q. Li, Y.H. Zhao, E.J. Lavernia, S.P. Ringer, T.G. Langdon, Y.T. Zhu, Scr. Mater. 64 (2011) 327–330.
[55] S. Ni, Y.B. Wang, X.Z. Liao, R.B. Figueiredo, H.Q. Li, S.P. Ringer, T.G. Langdon, Y.T. Zhu, Acta Mater. 60 (2012) 3181–3189.
[56] A. Stukowski, V.V. Bulatov, A. Arsenlis, Model. Simul. Mater. Sci. Eng. 20 (2012) 085007.
[57] F. Sansoz, Acta Mater. 59 (2011) 3364–3372.
[58] A. Stukowski, Model. Simul. Mater. Sci. Eng. 18 (2010) 015012.
[59] A.T. Jennings, C. Gross, F. Greer, Z.H. Aitken, S.W. Lee, C.R. Weinberger, J.R. Greer, Acta Mater. 60 (2012) 3444–3455.
[60] Y. Hu, L. Shu, Q. Yang, W. Guo, P.K. Liaw, K.A. Dahmen, J.M. Zuo, Commun. Phys. 1 (2018) 61.
[61] F. Shimizu, S. Ogata, J. Li, Mater. Trans. 48 (2007) 2923–2927.
[62] Z.J. Zhang, H.W. Sheng, Z.J. Wang, B. Gludovatz, Z. Zhang, E.P. George, Q. Yu, S.X. Mao, R.O. Ritchie, Nat. Commun. 8 (2017) 14390.
[63] Y. Xiao, Y. Zou, A.S. Sologubenko, R. Spolenak, J.M. Wheeler, Mater. Des. 193 (2020) 108786.
[64] L. Dupuy, M.C. Fivel, Acta Mater. 50 (2002) 4873–4885.
[65] E. Rodary, D. Rodney, L. Proville, Y. Bréchet, G. Martin, Phys. Rev. B 70 (2004) 054111.
[66] H.D. Fan, Q.Y. Wang, J.A. El-Awady, D. Raabe, M. Zaiser, Nat. Commun. 12 (2021) 1845.
[67] J.J. Gilman, Mech. Mater. 17 (1994) 83–96.
[68] D.L. Olmsted, L.G. HectorJr, W.A. Curtin, R.J. Clifton, Model. Simul. Mater. Sci. Eng. 13 (2005) 371–388.
[69] X.D. Xu, P. Liu, Z. Tang, A. Hirata, S.X. Song, T.G. Nieh, P.K. Liaw, C.T. Liu, M.W. Chen, Acta Mater. 144 (2018) 107–115.
[70] R.P. Zhang, S.T. Zhao, J. Ding, Y. Chong, T. Jia, C. Ophus, M. Asta, R.O. Ritchie, A.M. Minor, Nature 581 (2020) 283–287.
[71] J.C. Fisher, Acta Metall. 2 (1954) 9–10.
[72] C.G. Schön, Scr. Mater. 196 (2021) 113754.
[73] N.V. Malyar, J.S. Micha, G. Dehm, C. Kirchlechner, Acta Mater. 129 (2017) 91–97.
[74] J.S. Yu, J.L. Liu, J.X. Zhang, J.S. Wu, Mater. Lett. 60 (2006) 206–209.
[75] F. Hofmann, E. Tarleton, R.J. Harder, N.W. Phillips, P.W. Ma, J.N. Clark, I.K. Robinson, B. Abbey, W. Liu, C.E. Beck, Sci. Rep. 7 (2017) 45993.
[76] A.J. Cao, Y.G. Wei, S.X. Mao, Scr. Mater. 59 (2008) 219–222.
[77] N.L. Okamoto, S. Fujimoto, Y. Kambara, M. Kawamura, Z.M.T. Chen, H. Matsunoshita, K. Tanaka, H. Inui, E.P. George, Sci. Rep. 6 (2016) 35863.
[78] G. Richter, K. Hillerich, D.S. Gianola, R. Mönig, O. Kraft, C.A. Volkert, Nano Lett. 9 (2009) 3048–3052.
[79] C. Griesbach, S.J. Jeon, D.F. Rojas, M. Ponga, S. Yazdi, S. Pathak, N. Mara, E.L. Thomas, R. Thevamaran, Acta Mater. 214 (2021) 117020.
[80] Y. Feruz, D. Mordehai, Acta Mater. 103 (2016) 433–441.
[81] W.-S. Ko, A. Stukowski, R. Hadian, A. Nematollahi, J.B. Jeon, W.S. Choi, G. Dehm, J. Neugebauer, C. Kirchlechner, B. Grabowski, Acta Mater. 197 (2020) 54–68.
[82] P.J. Imrich, C. Kirchlechner, D. Kiener, G. Dehm, Scr. Mater. 100 (2015) 94–97.
[83] D.M. Norfleet, D.M. Dimiduk, S.J. Polasik, M.D. Uchic, M.J. Mills, Acta Mater. 56 (2008) 2988–3001.
[84] D. Kiener, A.M. Minor, Acta Mater. 59 (2011) 1328–1337.
[85] O. Kraft, P.A. Gruber, R. Mönig, D. Weygand, Annu. Rev. Mater. Res. 40 (2010) 293–317.
[86] S. Xu, Y.F. Guo, A.H.W. Ngan, Int. J. Plast. 43 (2013) 116–127.
[87] E. Rabkin, H.S. Nam, D.J. Srolovitz, Acta Mater. 55 (2007) 2085–2099.
[88] S. Zheng, S. Shinzato, S. Ogata, S.X. Mao, J. Mech. Phys. Solids 158 (2022) 104687.
[89] L. Fu, C. Yang, R. Wei, X. Pei, J. Teng, D. Kong, Y. Lu, Y. Guo, T. Liu, Y. Hu, B. Yin, Z. Zhang, A. Li, L. Wang, X. Han, Mater. Today Nano 15 (2021) 100123.
[90] Y.N. Cui, Z.L. Liu, Z.J. Wang, Z. Zhuang, J. Mech. Phys. Solids 89 (2016) 1–15.